

Supporting Information for

Climatic controls on interannual mass balance of Arctic glaciers and ice caps

Xiaojun Ma¹, Matt A. King^{2,3}, Jonathan L. Bamber^{4,5}, Bin Liu⁶, Wenke Sun¹, Qiuyu Wang^{1,4}

5 ¹State Key Laboratory of Earth System Numerical Modeling and Application, College of Earth and Planetary Sciences, University of Chinese Academy of Sciences, Beijing, 100049, China

²School of Geography, Planning, and Spatial Sciences and Institute for Marine and Antarctic Studies, University of Tasmania, Hobart, TAS, 7001, Australia

³The Australian Centre for Excellence in Antarctic Science, University of Tasmania, Hobart, TAS, 7001, Australia

10 ⁴Bristol Glaciology Centre, School of Geographical Sciences, University of Bristol, BS8 1SS, UK

⁵Chair of Data Science in Earth Observation, Department of Aerospace and Geodesy, Technical University of Munich, Munich, 80333, Germany

⁶School of Aeronautic Engineering, Changsha University of Science and Technology, Changsha, 410114, China

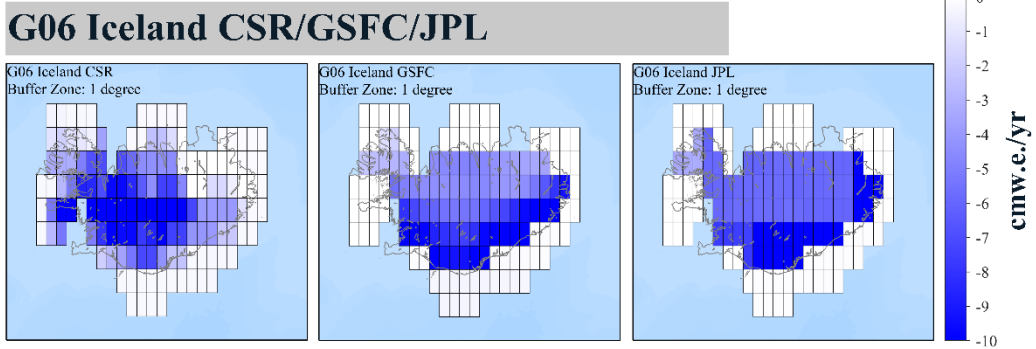
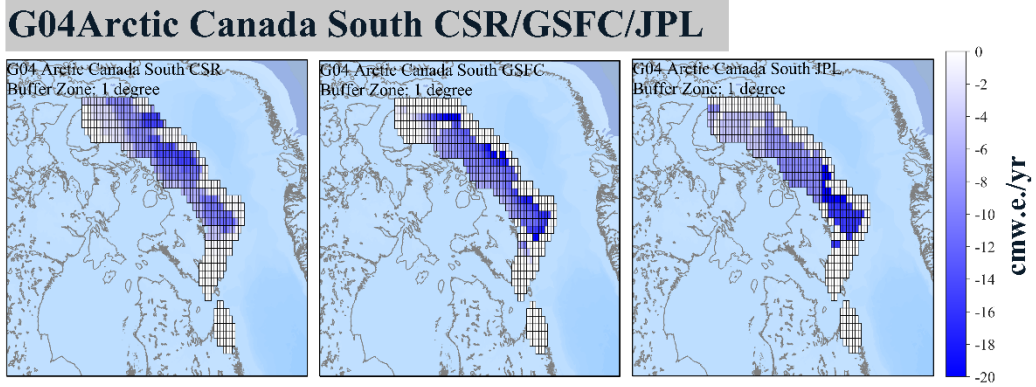
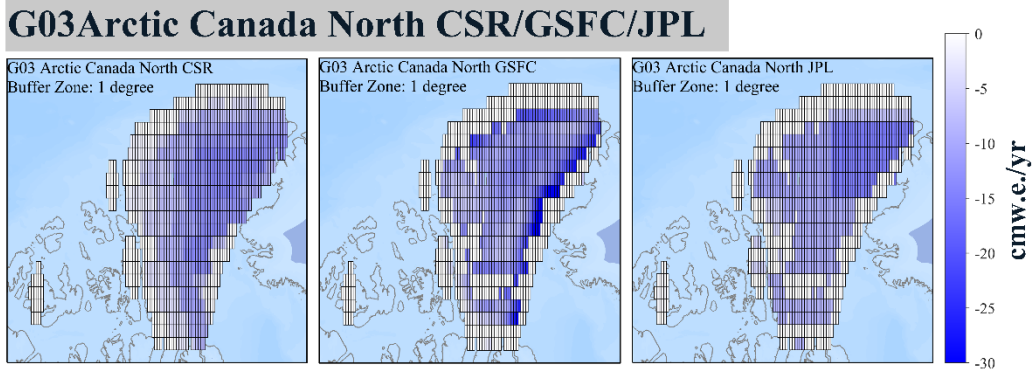
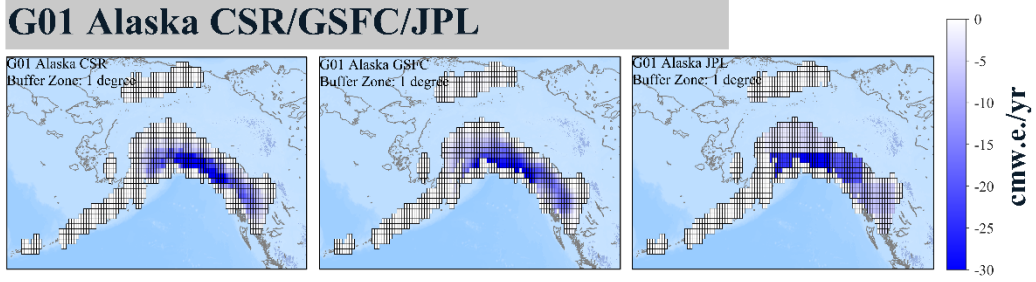
Correspondence to: Qiuyu Wang (wangqiuyu@ucas.ac.cn)

15 **This file includes:**

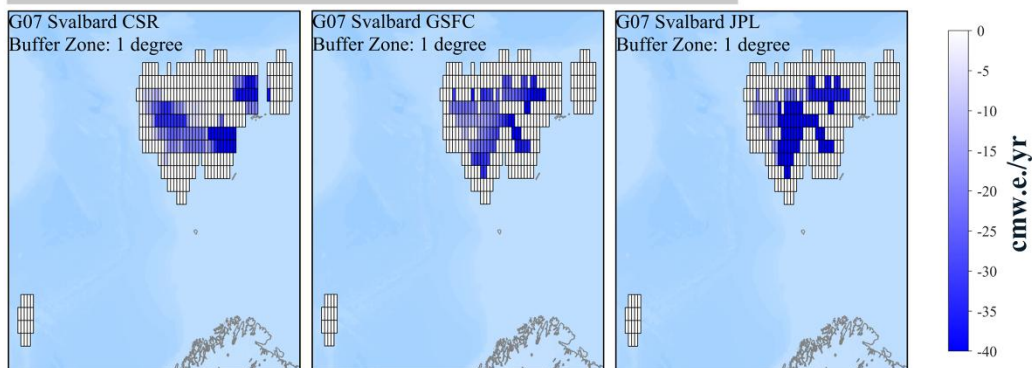
Figures S1 to S27

Tables S1 to S7

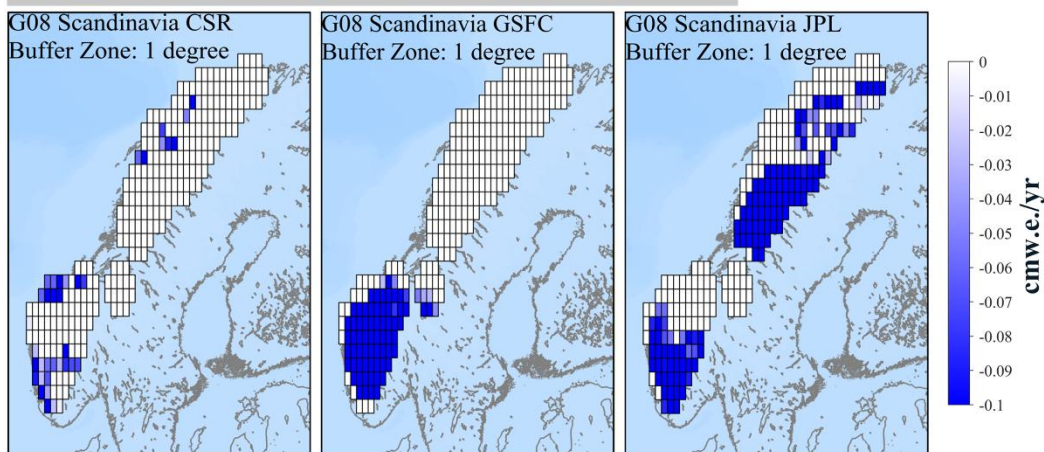
SI Reference



G07 Svalbard CSR/GSFC/JPL



G08 Scandinavia CSR/GSFC/JPL



G09 Russian Arctic CSR/GSFC/JPL

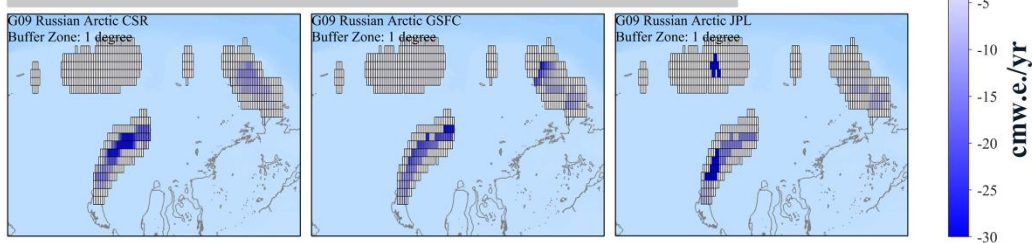
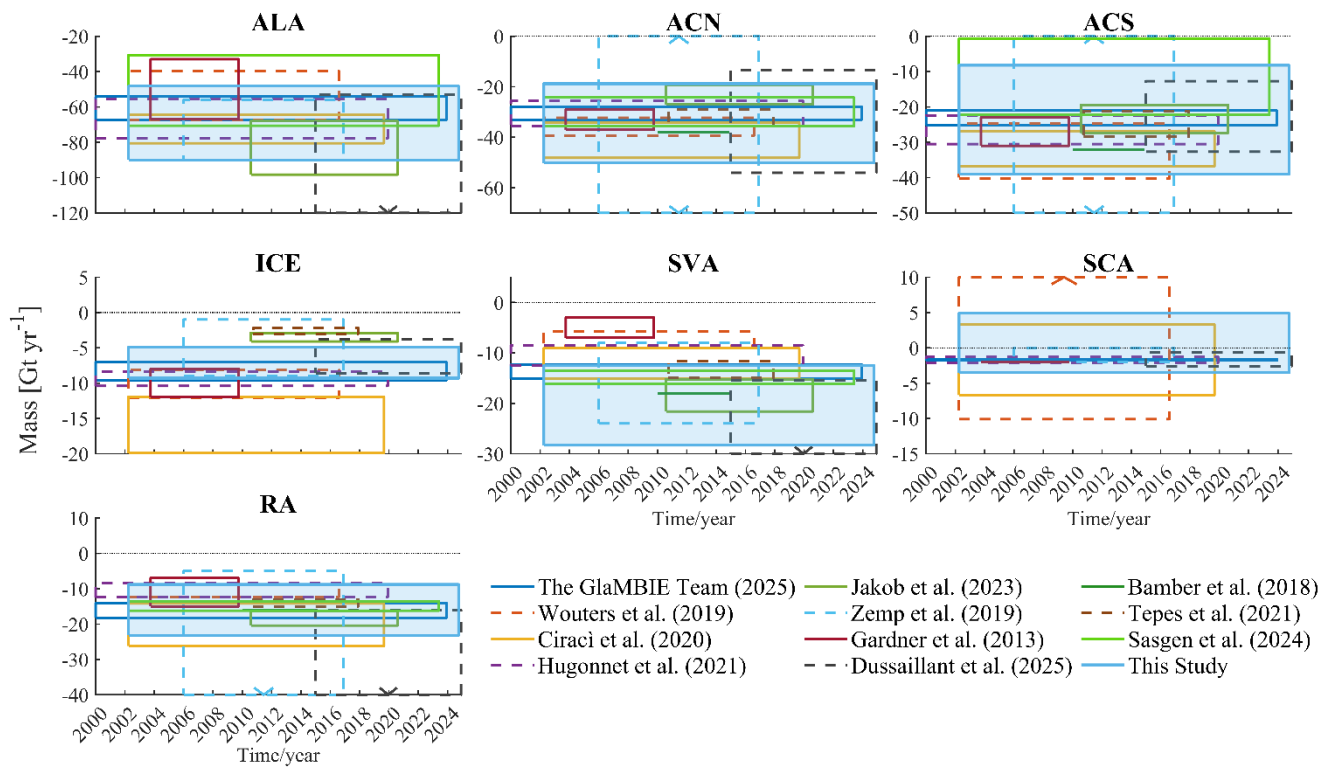
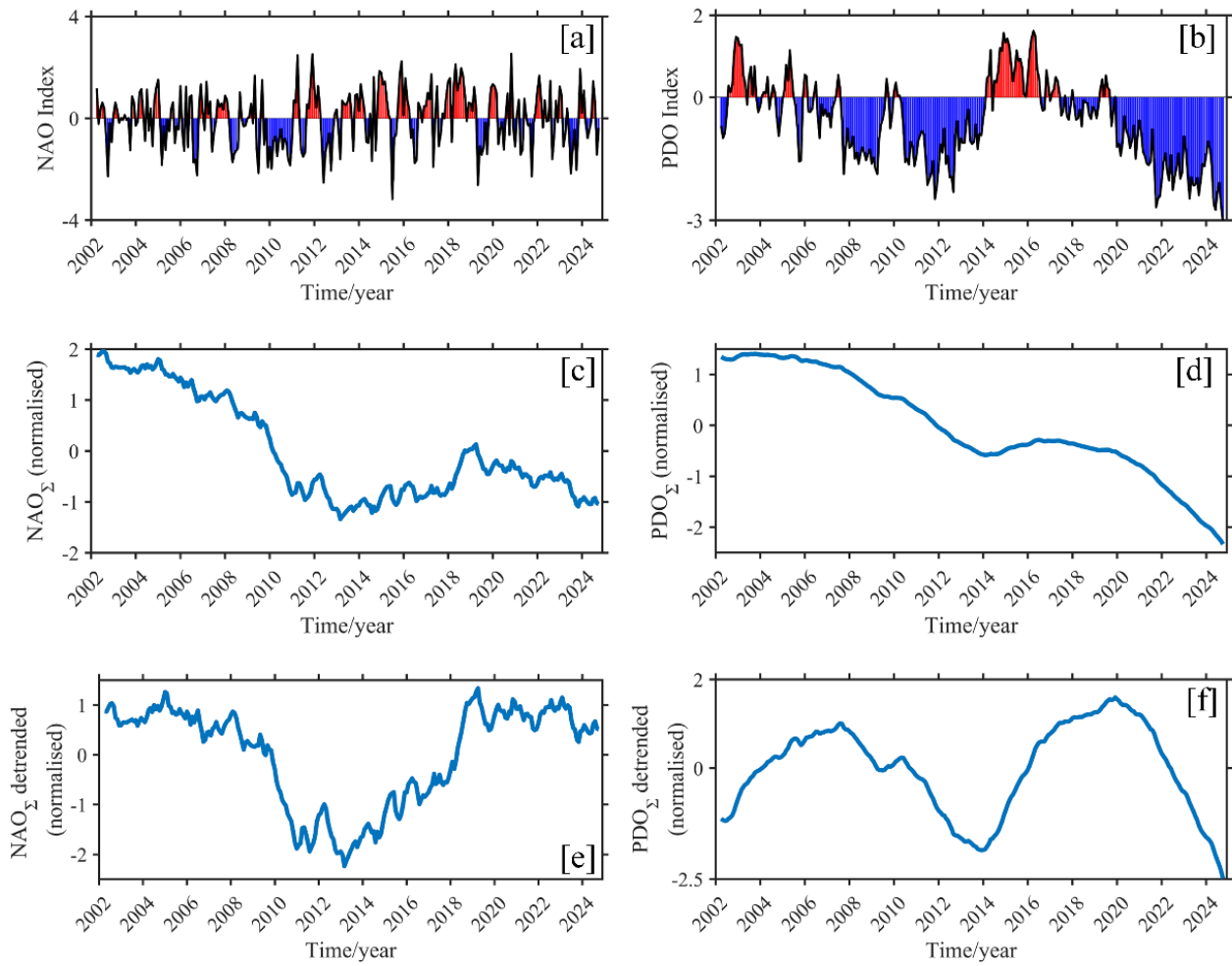


Figure S1: Spatial trends of GRACE Mascon solutions across selected glacier and ice-cap regions. Shown are the spatial masks used to delineate the major global glacier and ice-cap complexes, including the Arctic regions (G01, G03, G04, G06–G09). Based on the Randolph Glacier Inventory version 7.0, a 1° buffer was applied to define the final glacier-specific regional masks. Blue shading indicates glacier-covered grid cells, with color intensity representing the trend in glacier mass change observed during the GRACE observation period.

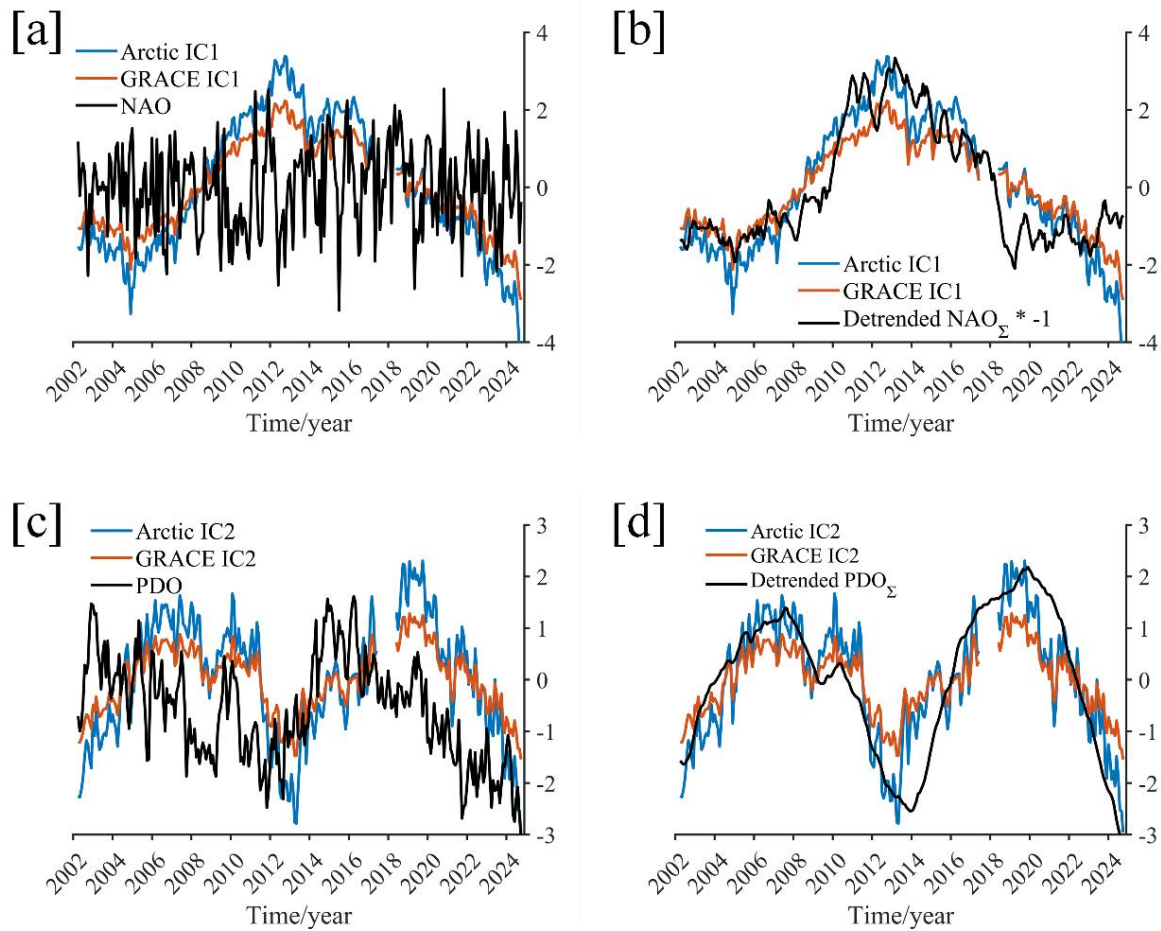


30

Figure S2: Comparison of Arctic glacier regional mass-balance estimates across studies and observation periods. Arctic glacier mass balance is shown as boxes representing the mean value over each study period, with box width indicating the time span of the estimate and box height indicating the associated uncertainty (95% CI). Our GRACE/GRACE-FO-based estimates for the satellite period are compared with published regional estimates from earlier studies. Panels show results for ALA, ACN, ACS, ICE, SVA, SCA and RA.



35 **Figure S3: Comparative analysis of PDO and NAO climate indices. Panels (a–b) show the original standardized versions of each index during the GRACE observation period. Panels (c–d) show the cumulatively summed indices. Panels (e–f) show depicts their detrended and normalized forms. The climatological reference period is 1971–1999.**



40 **Figure S4: Comparison between ICA-derived temporal components and climate indices before and after cumulative summation. Panels (a–b) compare the first independent component (IC) of interannual glacier mass anomalies obtained from ICA decomposition, GRACE IC1 (global) and Arctic IC1 (Arctic), with both the original and cumulative NAO index time series. Panels (c–d) similarly compare GRACE IC2 and Arctic IC2 with the original and cumulative PDO index time series.**

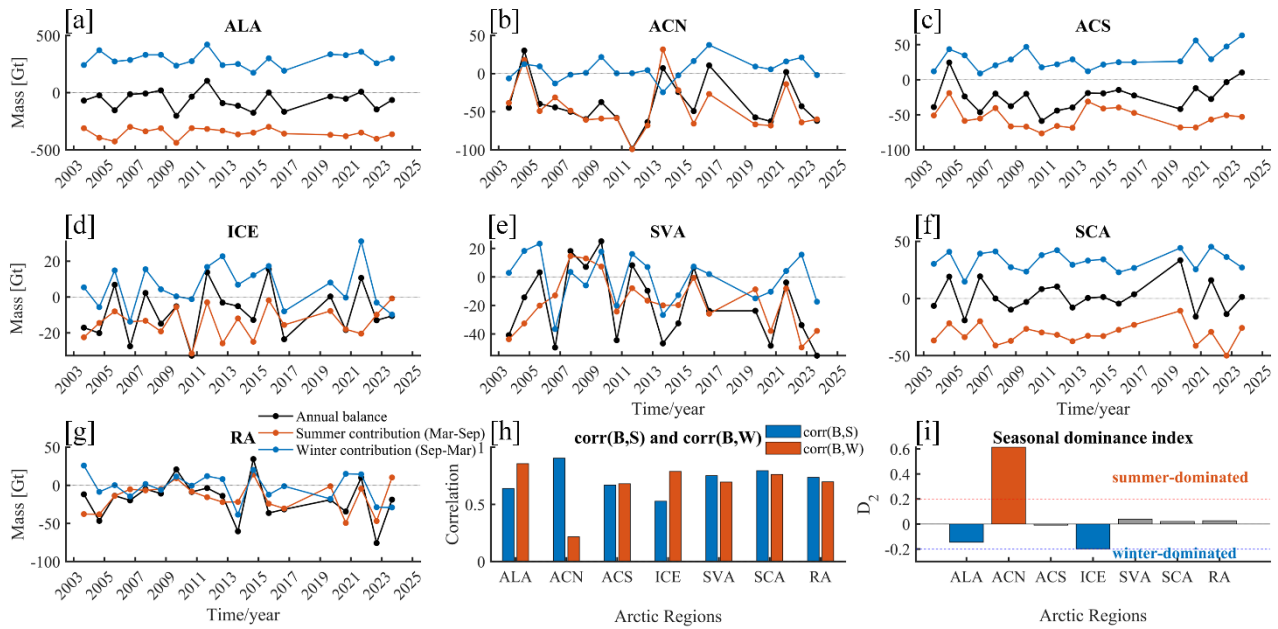
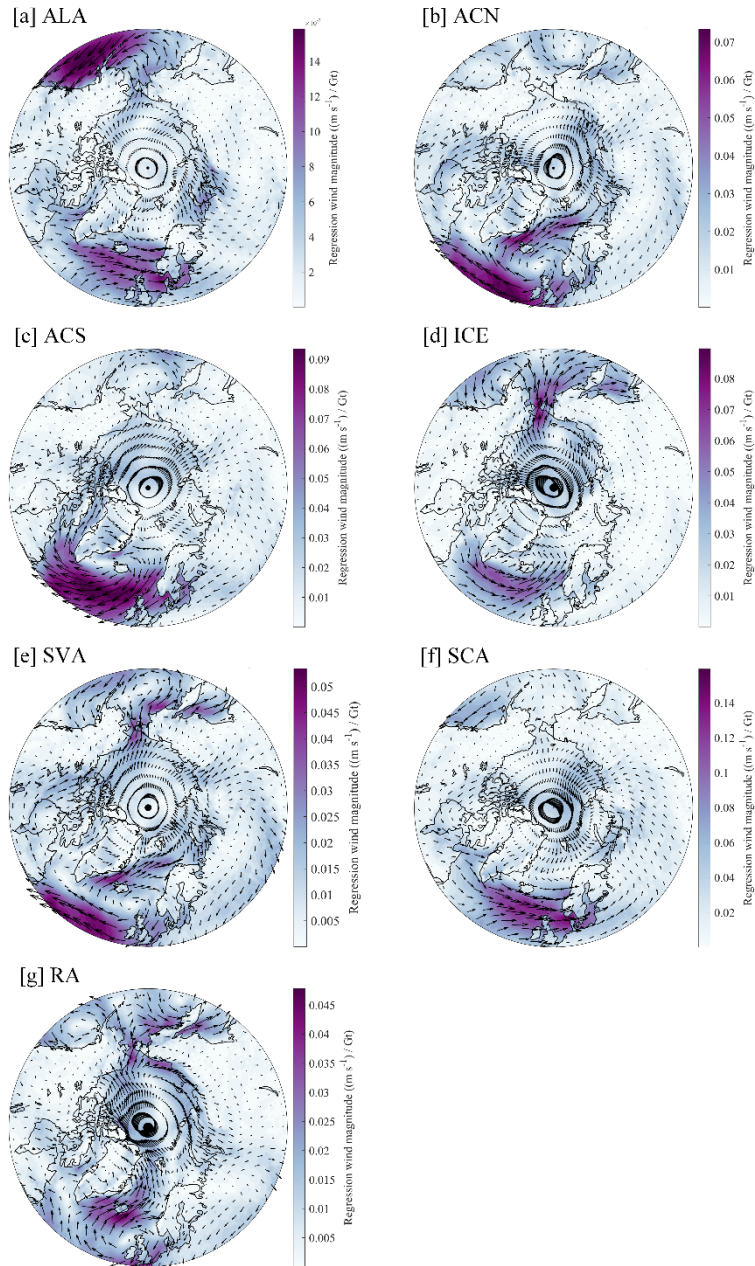


Figure S5: Annual balance and seasonal contributions across Arctic glacier regions. Annual balance was defined from March to March of the following year, so that the full melt season is included within a single balance year. For each region, the seasonal analysis was based on 19 valid annual balance years, excluding years affected by the GRACE/GRACE-FO mission gap. The annual balance was partitioned into summer and winter contributions. Panels a–g show the annual balance together with its summer and winter contributions for each region, panel h shows the correlations of annual balance with the two seasonal contributions, and panel i summarizes their relative influence using the seasonal dominance index. Panels a–g show results for ALA, ACN, ACS, ICE, SVA, SCA and RA, respectively.

45

cold-season contribution vs DJF wind regression

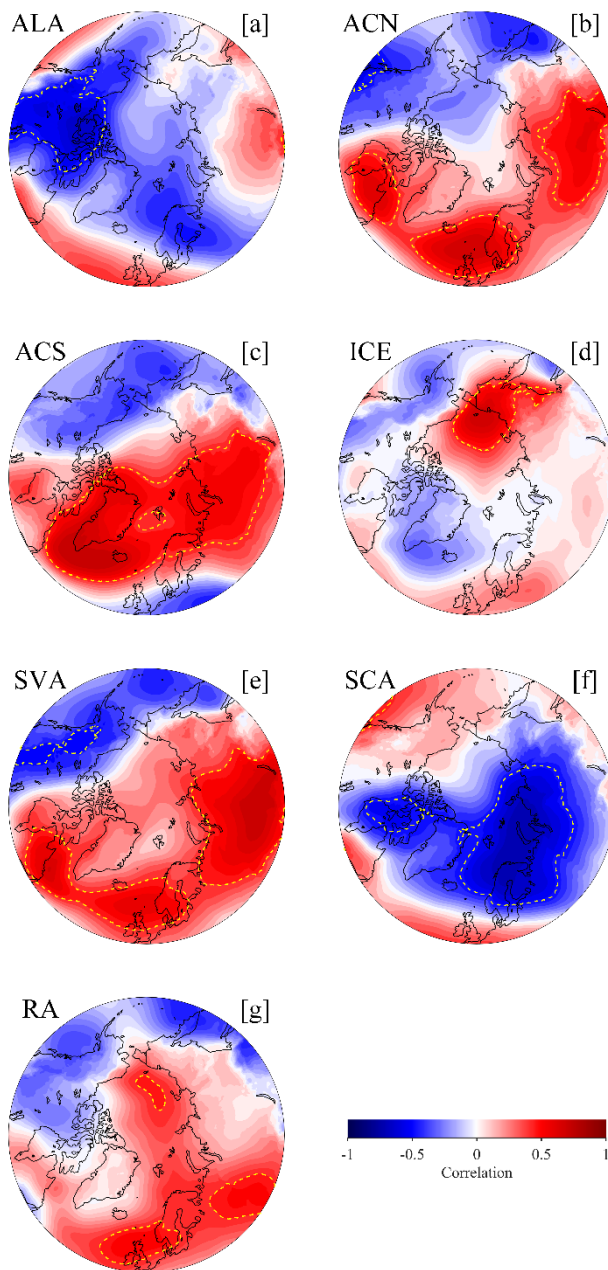


50

Figure S6: Regression of regional cold-season annual mass-balance contributions against DJF near-surface wind anomalies over the Arctic. Grid-point linear regressions of December–February (DJF) wind anomalies against the cold-season contribution in each Arctic glacier region. Arrows show the regression of the zonal and meridional wind components, and shading shows the corresponding regression wind magnitude. Monthly wind fields were referenced to the 1971–1999 climatology and then averaged to form DJF anomalies. The resulting patterns highlight region-dependent but spatially coherent cold-season circulation anomalies associated with interannual variability in glacier mass balance, including changes in the strength and direction of meridional and zonal flow across the Arctic. Panels a–g show results for ALA, ACN, ACS, ICE, SVA, SCA and RA, respectively.

55

cold-season contribution vs DJF SLP correlation



60 **Figure S7: Correlation of regional cold-season annual mass-balance contributions with DJF mean sea-level pressure (SLP) over**
the Arctic. Correlation (lag zero) of each region's cold-season contribution with DJF mean sea-level pressure (SLP) anomalies
derived from reanalysis data. Monthly SLP fields were referenced to the 1971–1999 climatology and then averaged to form DJF
anomalies. Yellow dotted contours indicate areas of statistical significance ($P < 0.05$), accounting for autocorrelation in the
GRACE-derived mass-balance time series through a reduction in effective degrees of freedom. The maps highlight region-
dependent but spatially coherent Arctic circulation patterns associated with interannual variability in cold-season glacier mass
65 balance. Panels a–g show results for ALA, ACN, ACS, ICE, SVA, SCA and RA, respectively.

cold-season contribution vs DJF precipitation correlation

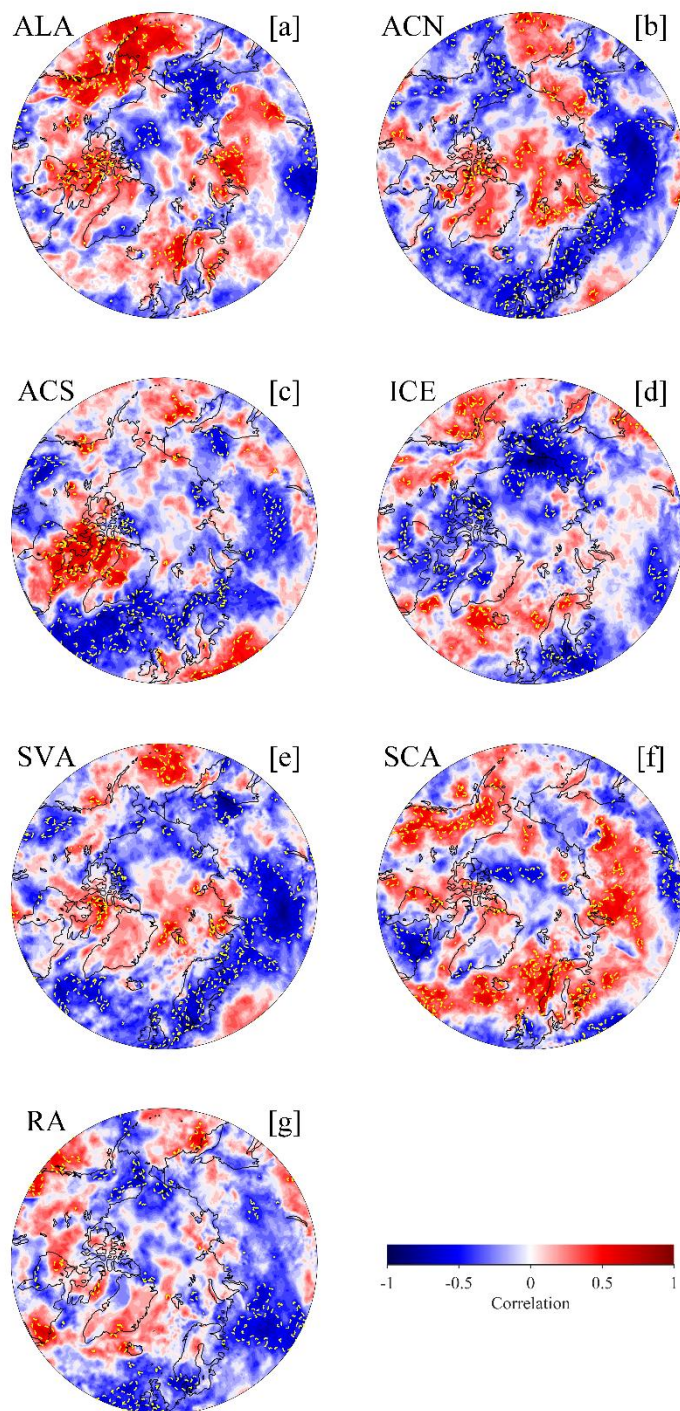


Figure S8: Correlation of regional cold-season annual mass-balance contributions with DJF precipitation over the Arctic.

warm-season contribution vs JJA wind regression

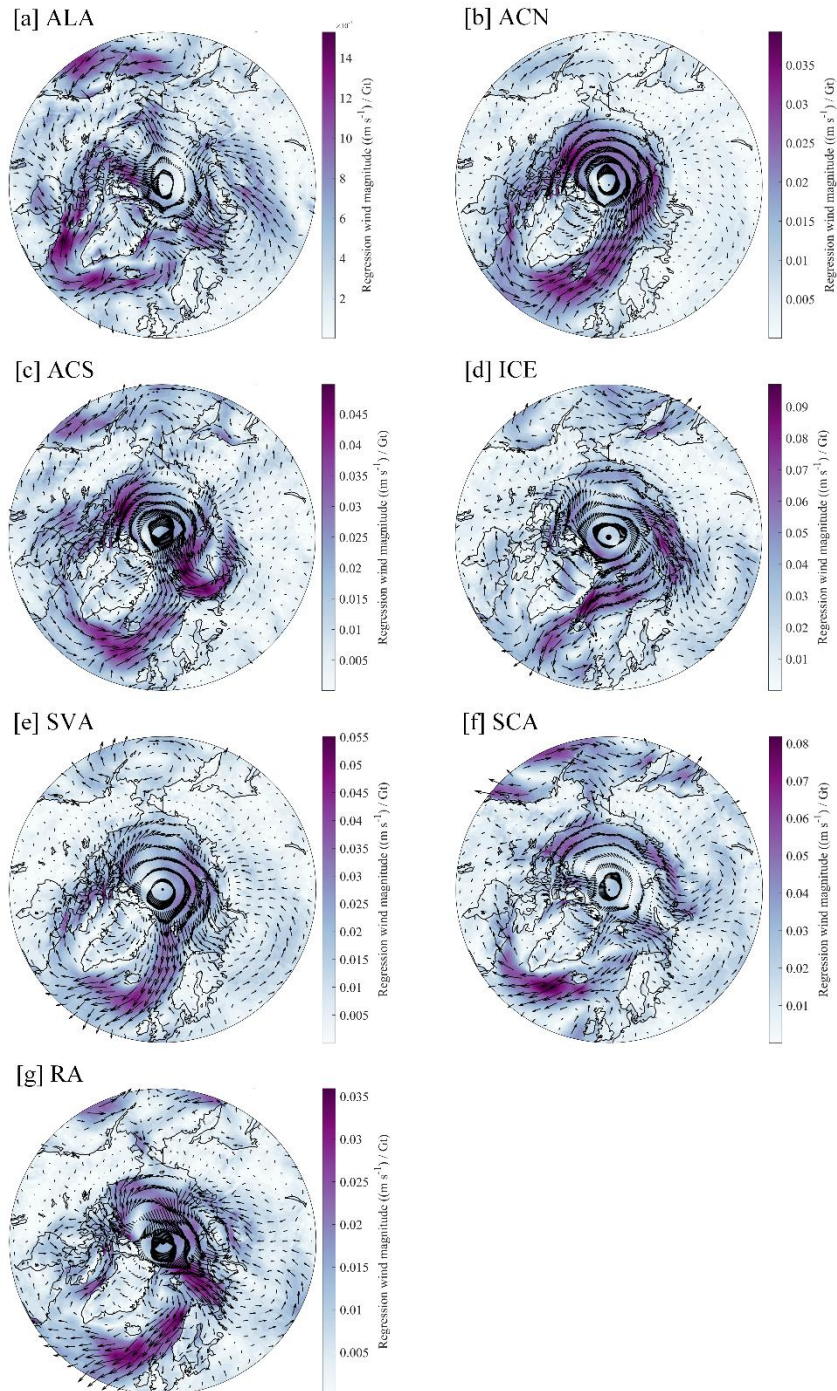


Figure S9: Regression of regional warm-season annual mass-balance contributions against JJA near-surface wind anomalies over the Arctic.

warm-season contribution vs JJA SLP correlation

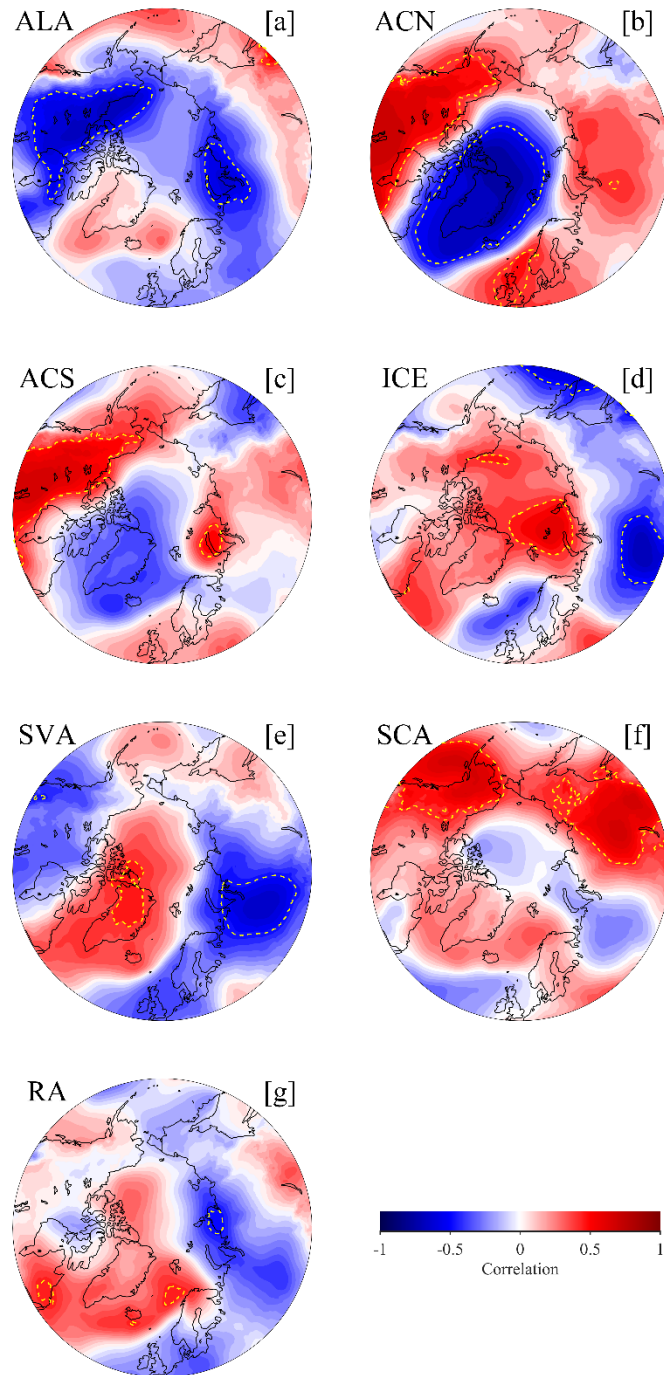
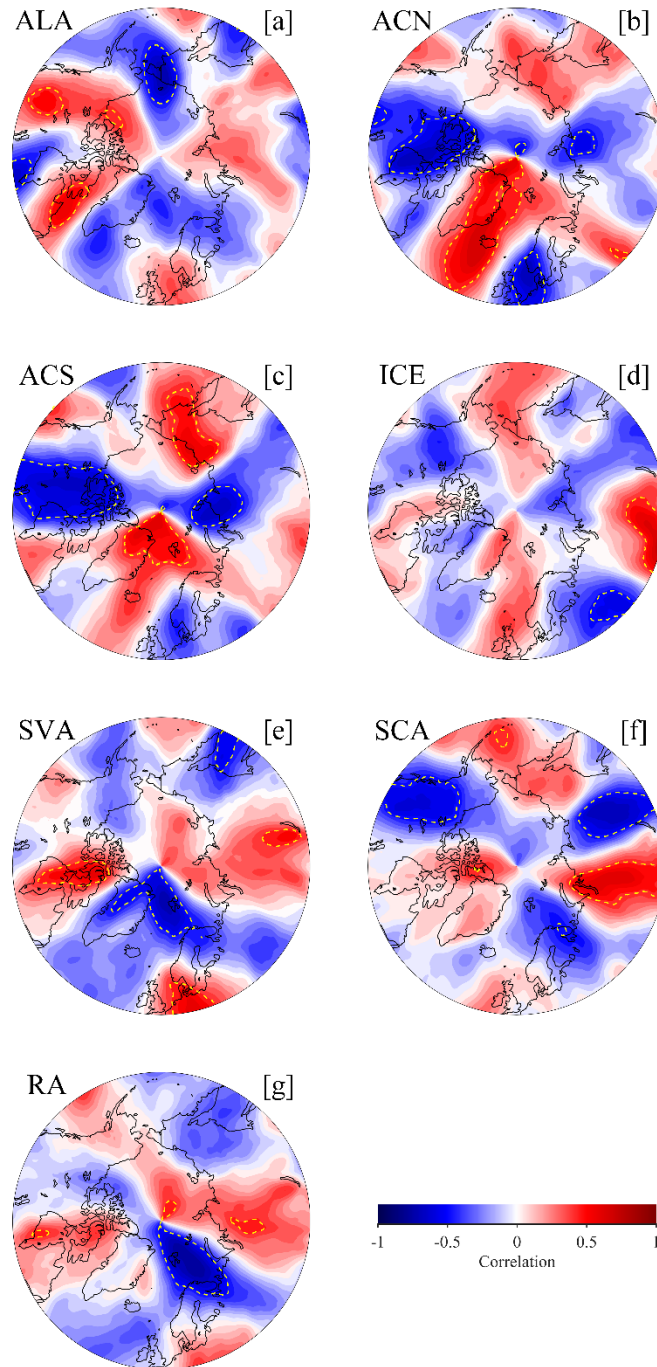


Figure S10: Correlation of regional warm-season annual mass-balance contributions with JJA mean sea-level pressure (SLP) over the Arctic.

warm-season contribution vs JJA NHF correlation



75 **Figure S11: Correlation of regional warm-season annual mass-balance contributions with JJA vertically integrated northward heat flux (NHF) over the Arctic.**

warm-season contribution vs JJA T_{2m} correlation

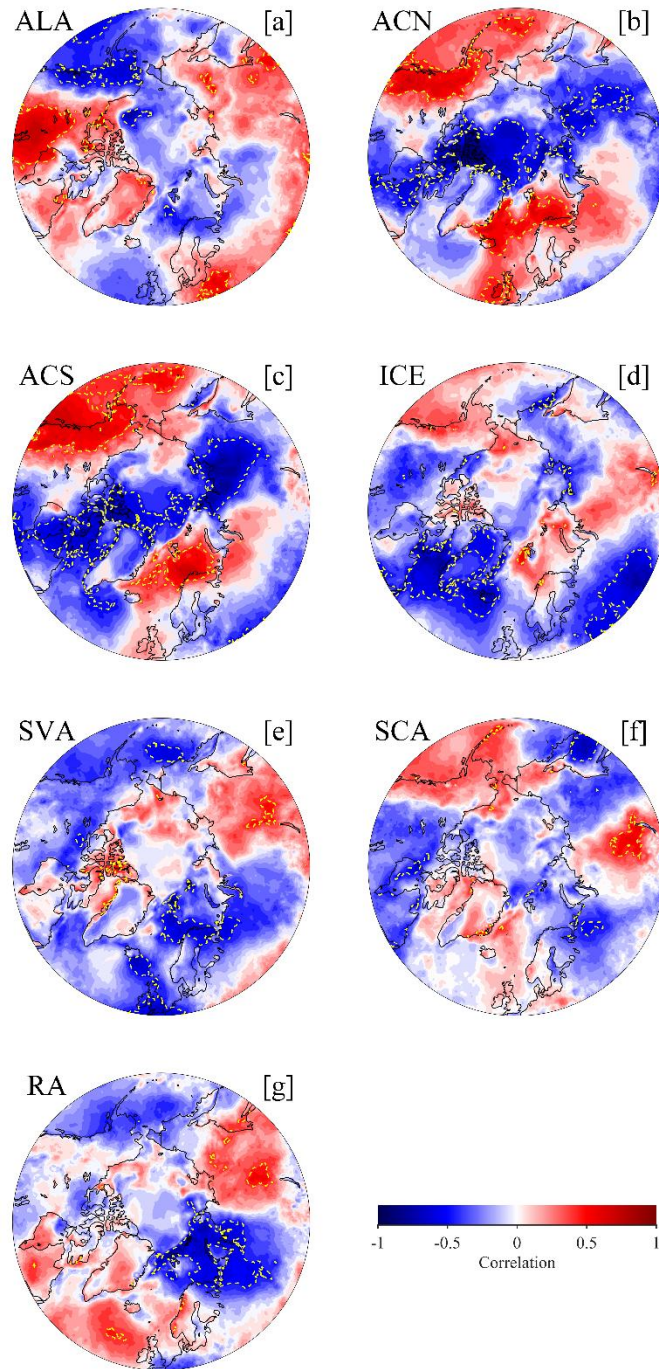
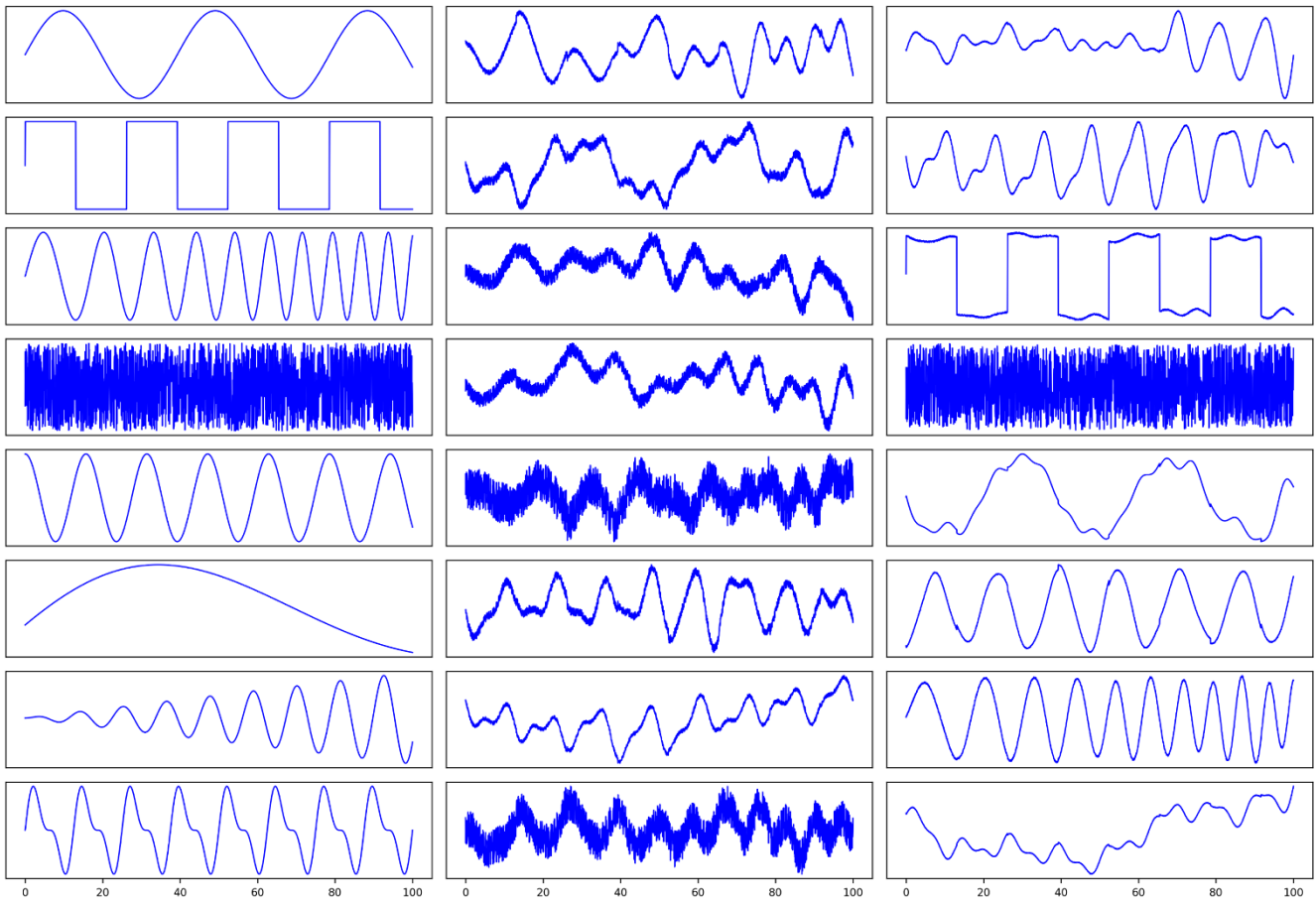


Figure S12: Correlation of regional warm-season annual mass-balance contributions with JJA 2 m air temperature (T_{2m}) over the Arctic.

[a] original source

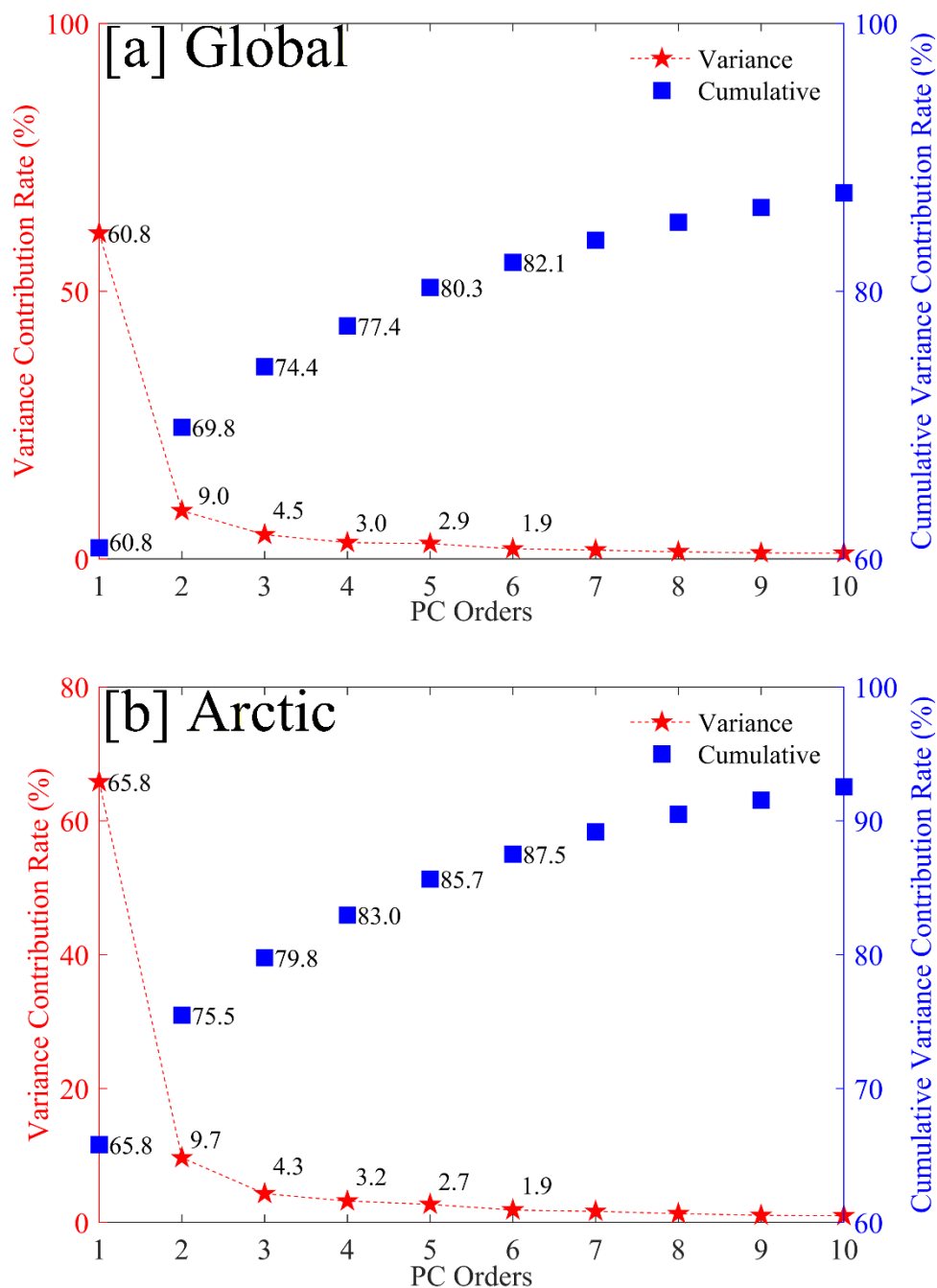
[b] mixed signals

[c] ICA separated signals

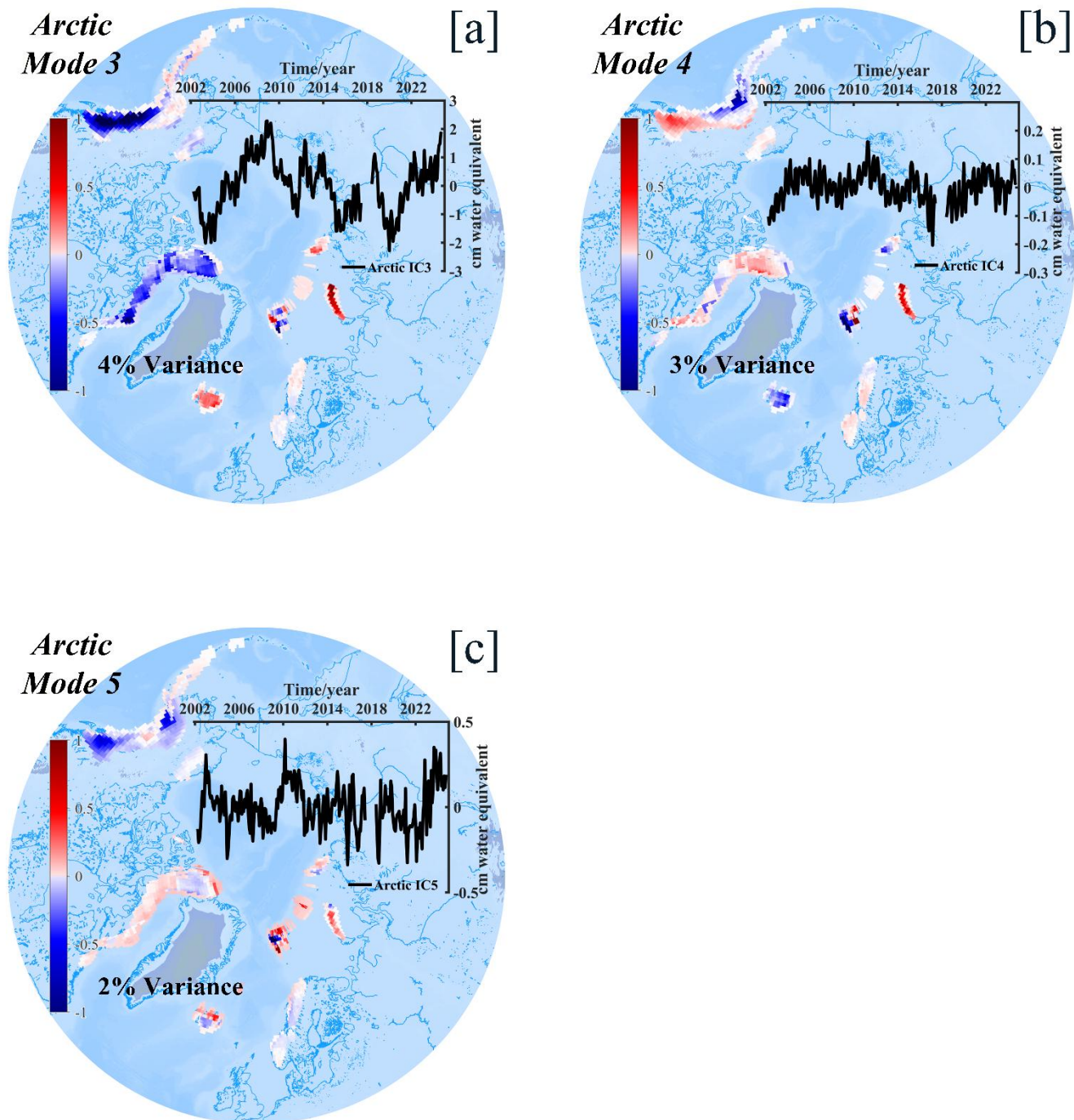


80

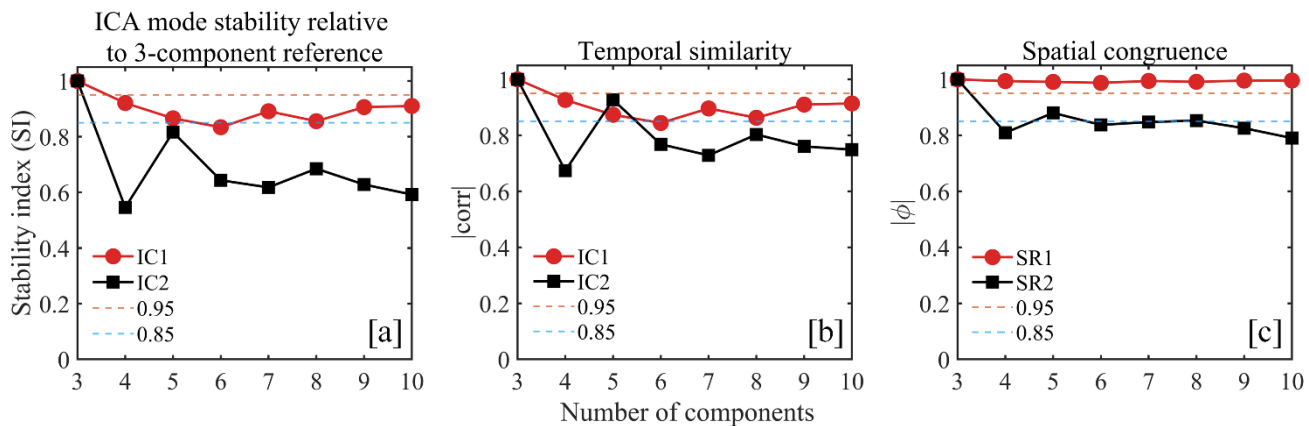
Figure S13: Demonstration of ICA decomposition. (a) Eight independent source signals used for simulation. (b) Linearly mixed observations derived from the sources. (c) Independent components reconstructed using the Fast-ICA method.



85 **Figure S14: Variance contributions of the first ten principal components at global and Arctic scales. The upper panels show the variance explained by the first ten principal components (PCs) of global glaciers and ice caps (GICs). The individual variance contribution (left y-axis, %) is indicated by red pentagrams and dashed lines, while the cumulative variance contribution (right y-axis, %) is shown by blue squares. The lower panels present the corresponding individual and cumulative variance contributions for the Arctic GIC time series.**



90 Figure S15: Secondary modes of Arctic glacier mass variability. Panels (a–c) show the third to fifth independent components (IC3–IC5) extracted from the detrended time series of glacier and ice cap (GIC) mass changes across seven Arctic regions, along with the corresponding variance contribution of each component.



95 **Figure S16: Stability of the leading ICA modes across different numbers of retained components. a, Stability index (SI) of the first two ICA modes relative to the 3-component reference solution. b, Temporal similarity ($|\text{corr}|$) between the reference modes and the matched components from each decomposition. c, Spatial similarity ($|\phi|$) between the reference and matched modes.**

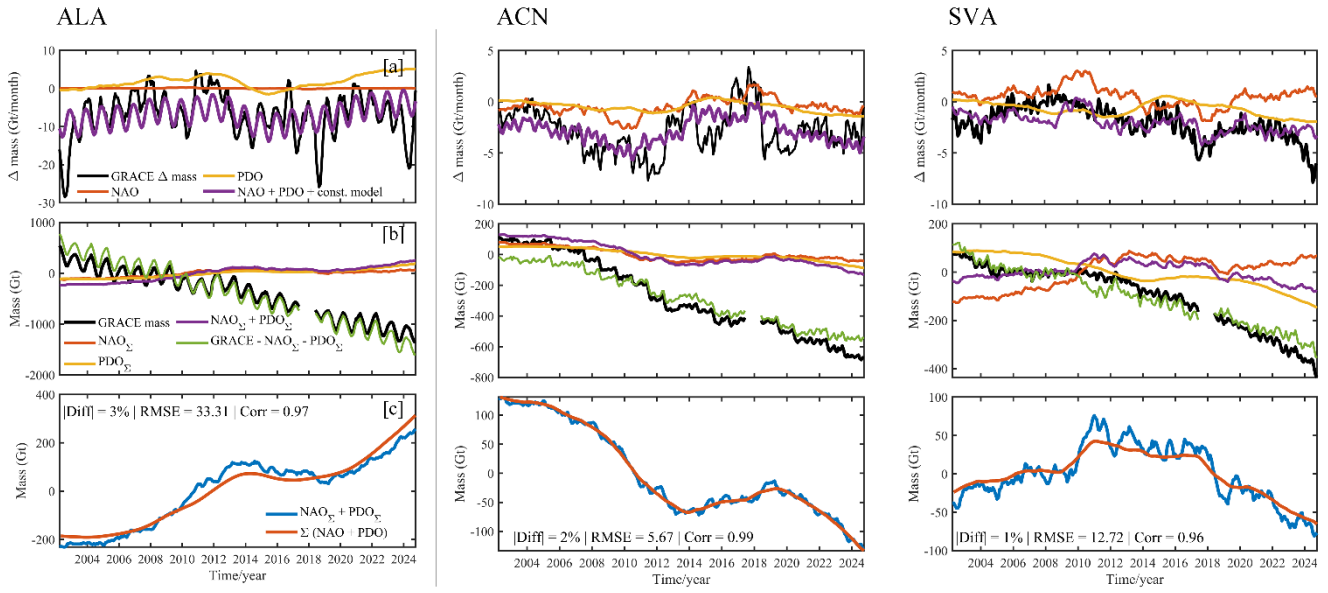
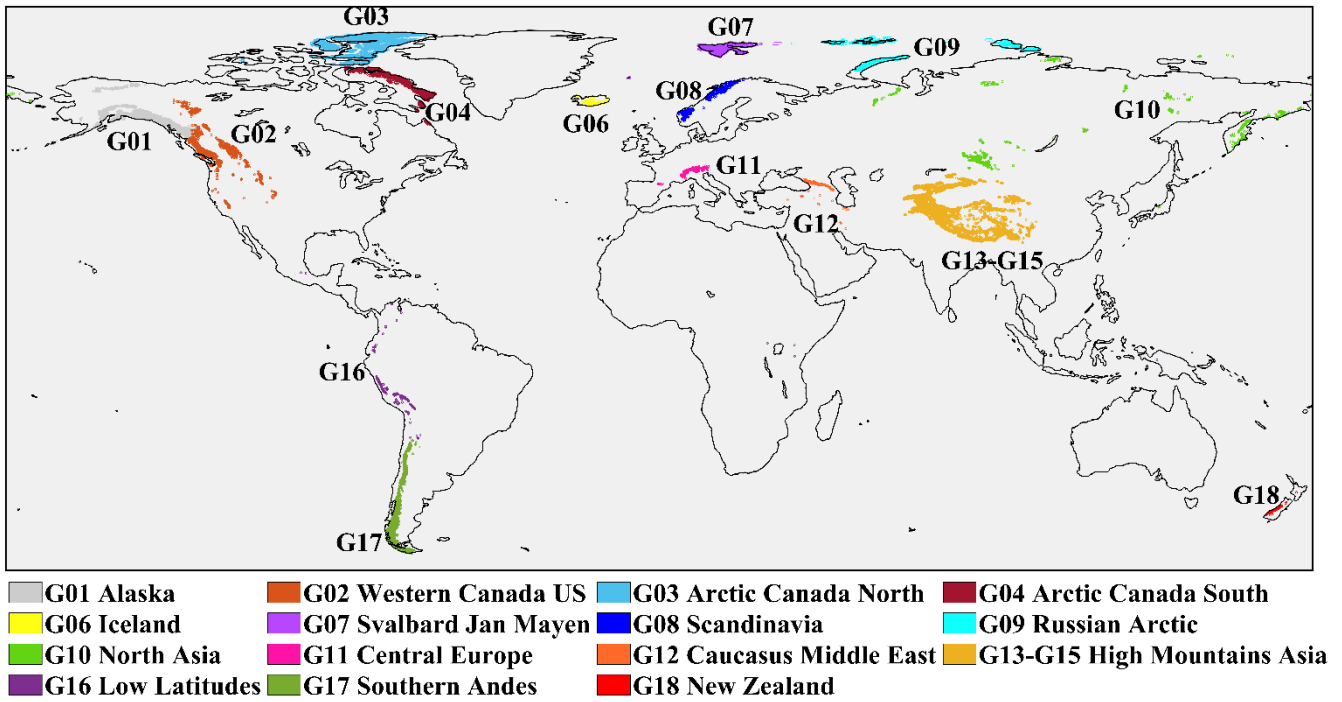
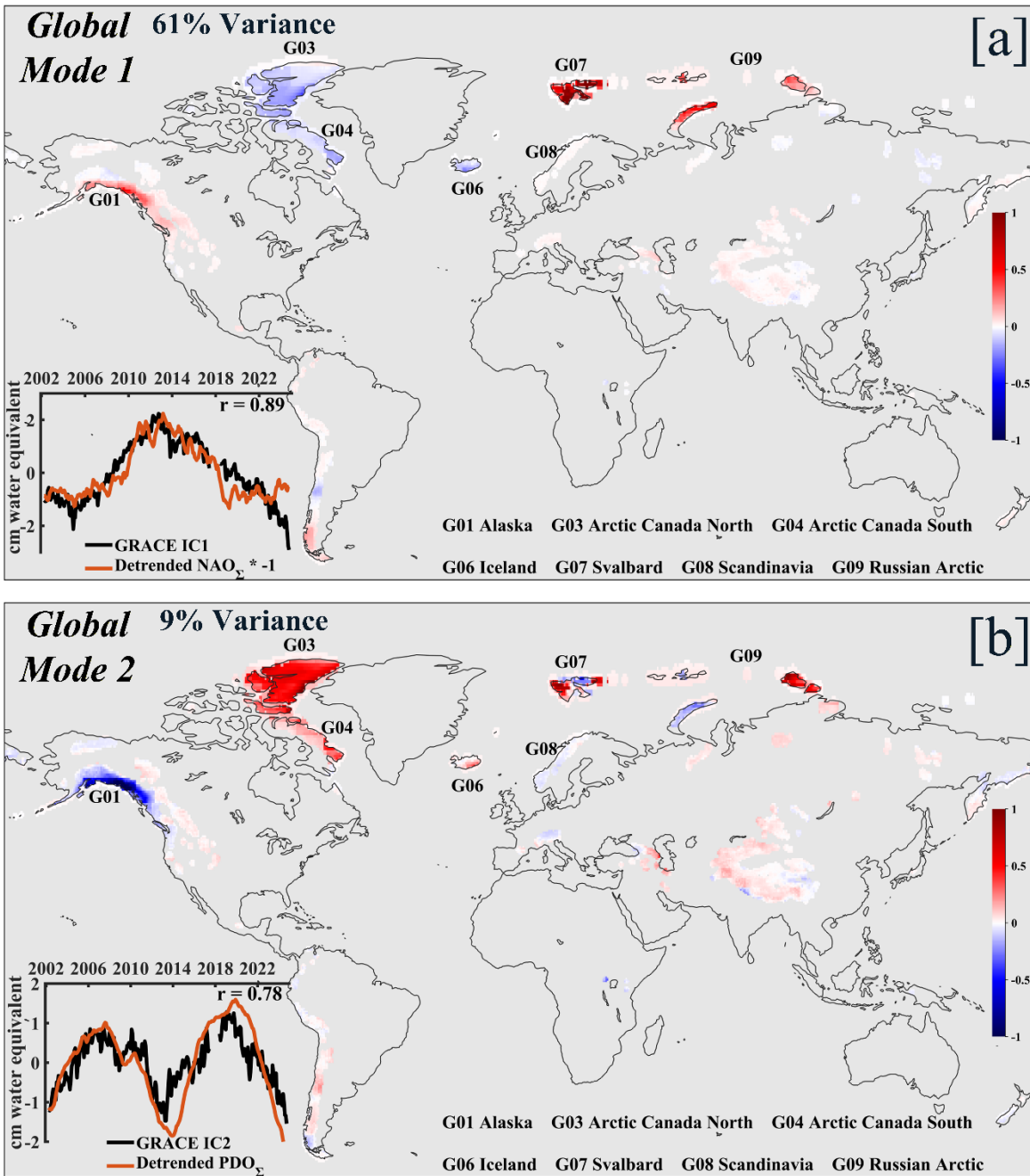


Figure S17: Results of multivariate regression using time-differenced GRACE/GRACE-FO mass anomalies for Alaska (ALA), Arctic Canada North (ACN) and Svalbard (SVA). Panel a shows the time-differenced GRACE/GRACE-FO data and the NAO and PDO components of the model fit to it (Equation 8). Panel b shows the GRACE/GRACE-FO mass-anomaly data with the cumulative sum of the NAO and PDO model components, and the residual after removing the NAO and PDO components of the model. Panel c compares the time-integrated NAO+PDO model with that estimated using undifferenced GRACE/GRACE-FO mass anomalies.

100



105 Figure S18: Locations of glaciers and ice caps from the Randolph Glacier Inventory version 7.0. Glaciers and ice caps are divided into 17 regions, with Central Asia (G13), South Asia West (G14), and South Asia East (G15) combined into a single region, High Mountain Asia (G13–G15).



110 Figure S19: Leading ICA modes in the global GRACE/GRACE-FO GIC regional record. Panels a–b show the first two ICA modes derived from detrended regional mass change time series from the global GIC record, explaining 61% and 9% of the interannual variance, respectively. Time series of the ICs are shown together with the detrended NAO_{Σ} and PDO_{Σ} indices. The Arctic subset comprises Alaska, Arctic Canada North, Arctic Canada South, Iceland, Svalbard, Scandinavia, and the Russian Arctic, corresponding to RGI regions G01, G03, G04, and G06–G09 (Fig. S18).

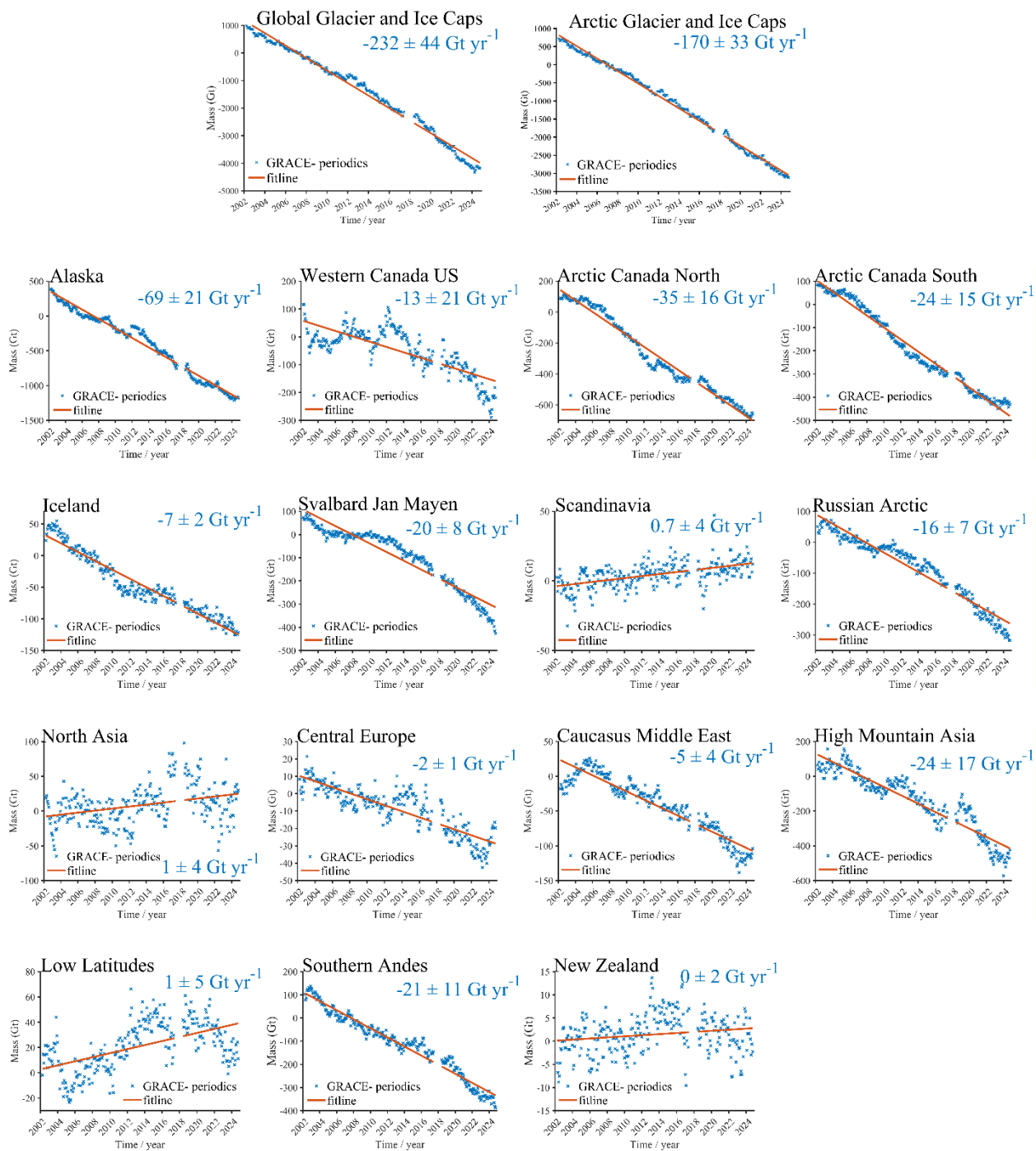


Figure S20: Global glacier mass change from April 2002 to October 2024. Shown are the glacier mass changes for 17 glacier regions since 2002. The annual mean rate (upper right of each panel, in Gt yr⁻¹) is indicated. Blue curves represent the regional glacier mass time series after removal of the seasonal component, and orange lines denote the linear trends estimated using least-squares fitting.



120

Figure S21: Nonlinear glacier mass variability. Time series of glacier mass change (blue stars) for Alaska, Arctic Canada North, Arctic Canada South, Iceland, Svalbard, Scandinavia, and the Russian Arctic. The time series are shown after removing the linear and periodic terms obtained from the multiple linear regression. The NAO_Σ and PDO_Σ components of the model are shown separately, together with their combined sum (solid line). The inset text indicates the partial variance (R^2) explained by NAO_Σ and

125

PDO_Σ together, as well as by each component individually.

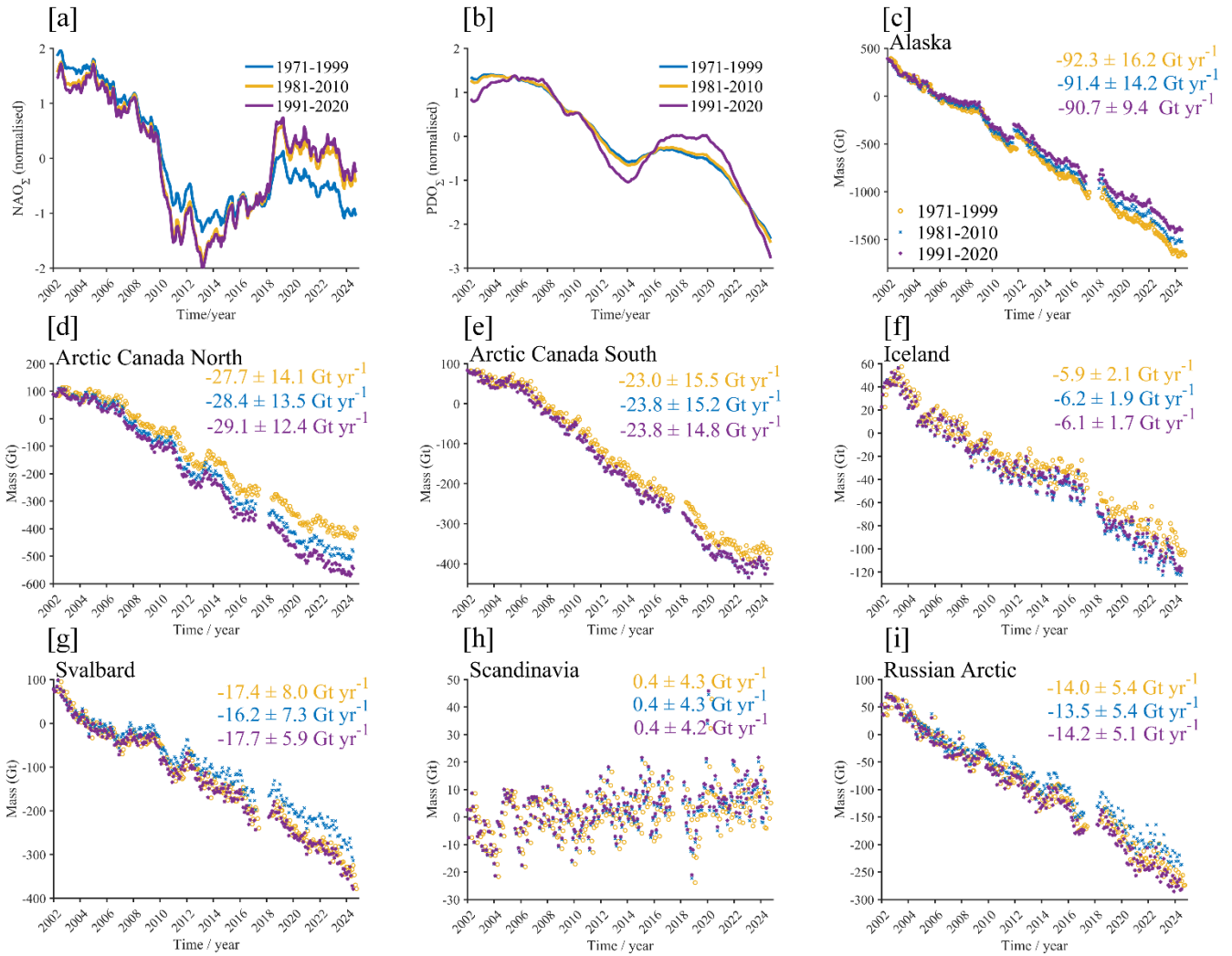
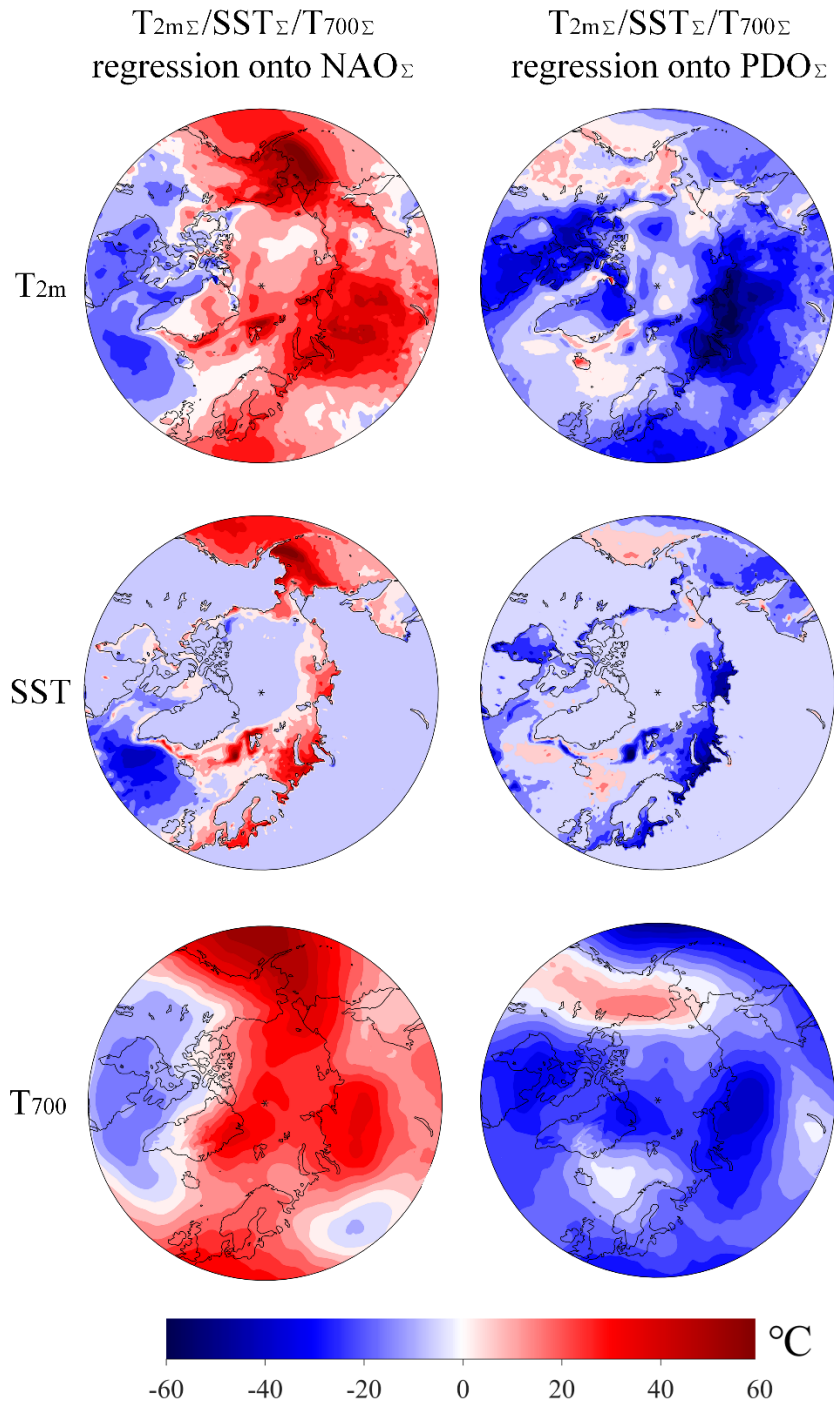


Figure S22: Sensitivity of cumulative NAO and PDO indices and regression-derived residual trends to the choice of climatological reference period. Panels a and b show the cumulative NAO (NAO_{Σ}) and PDO (PDO_{Σ}) indices, respectively, normalised over the GRACE/GRACE-FO period (2002–2024), after defining monthly anomalies relative to three climatological reference periods: 1971–1999, 1981–2010 and 1991–2020. Coloured curves denote the different reference periods. Panels c–i show the corresponding residual linear trends obtained from the regression model that includes NAO_{Σ} and PDO_{Σ} for the seven Arctic glacier regions: Alaska (ALA; c), Arctic Canada North (ACN; d), Arctic Canada South (ACS; e), Iceland (ICE; f), Svalbard (SVA; g), Scandinavia (SCA; h) and Russian Arctic (RA; i).

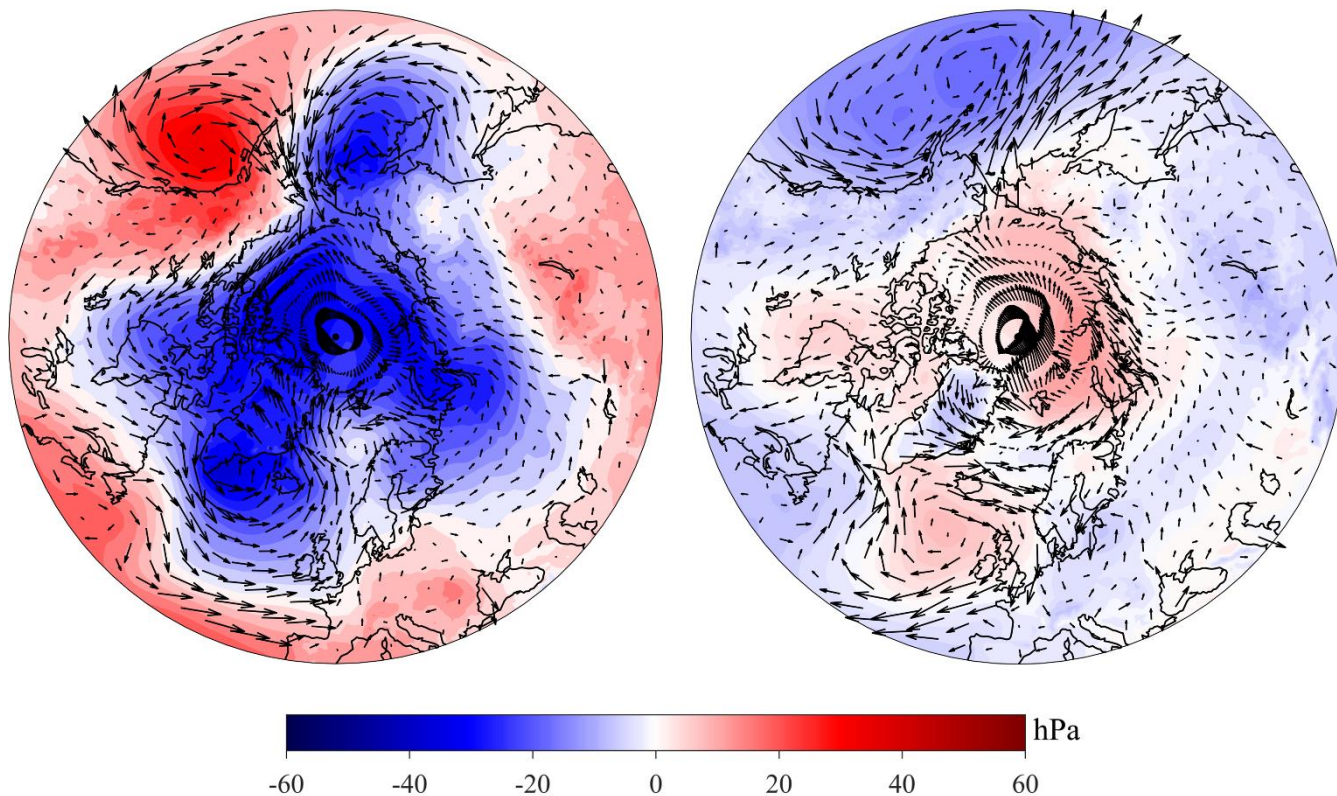
130



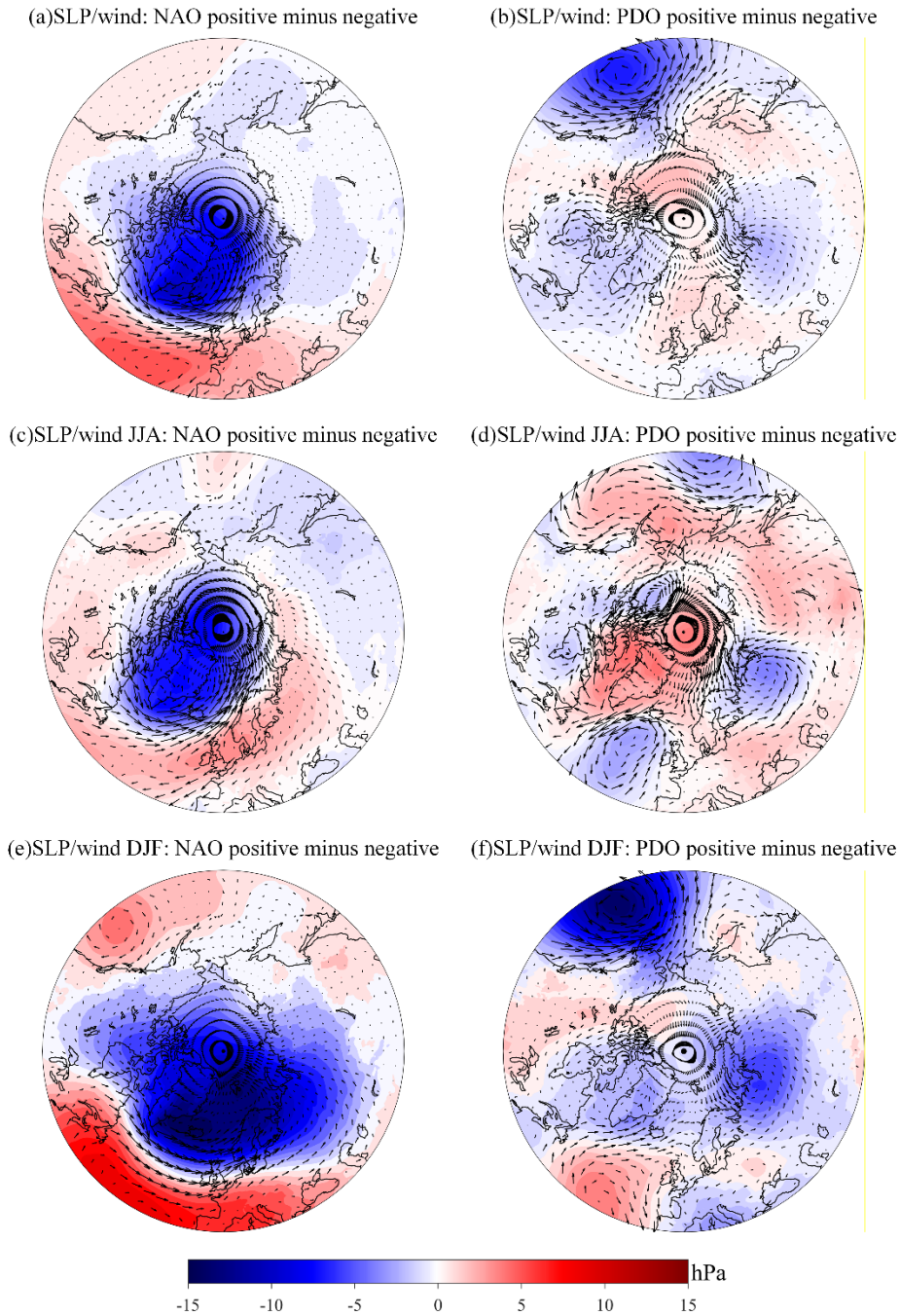
135 **Figure S23: Decadal variability in temperature.** Maps show the regression relationships between the cumulative North Atlantic Oscillation (NAO_{Σ}) and Pacific Decadal Oscillation (PDO_{Σ}) indices and the cumulative anomalies of surface air temperature ($T_{2m\Sigma}$), sea surface temperature (SST_{Σ}), and 700-hPa air temperature ($T_{700\Sigma}$) from ERA5 reanalysis. The climatological reference period is 1971–1999.

(a) $SLP_{\Sigma}/wind_{\Sigma}$ regression onto NAO_{Σ}

(b) $SLP_{\Sigma}/wind_{\Sigma}$ regression onto PDO_{Σ}



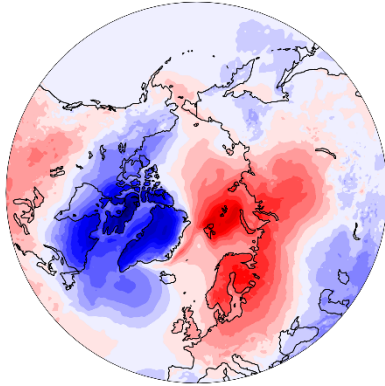
140 **Figure S24: Decadal variability in wind.** Maps show the regression relationships between the cumulative North Atlantic Oscillation (NAO_{Σ}) and Pacific Decadal Oscillation (PDO_{Σ}) indices and the cumulative anomalies of sea level pressure (SLP_{Σ}), and 10 m winds ($wind_{\Sigma}$) from ERA5 reanalysis. The climatological reference period is 1971–1999.



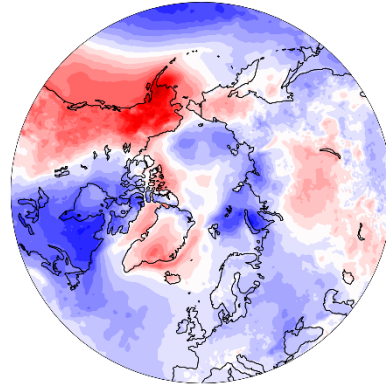
145

Figure S25: Anomalies of ERA5 10 m winds and sea-level pressure related to unsummed NAO and PDO indices. ERA5 10 m wind anomalies are shown as vectors and sea-level pressure anomalies as shading over the Arctic for 2002–2024. Panels show composite differences between positive and negative NAO phases for all seasons (a), boreal summer (c) and boreal winter (e), and between positive and negative PDO phases for all seasons (b), boreal summer (d) and boreal winter (f). Positive and negative phases are defined as months when the normalized NAO or PDO index is greater than +0.5 or less than -0.5 (Fig. S27), respectively. Anomalies are calculated relative to the 1971–1999 monthly climatology.

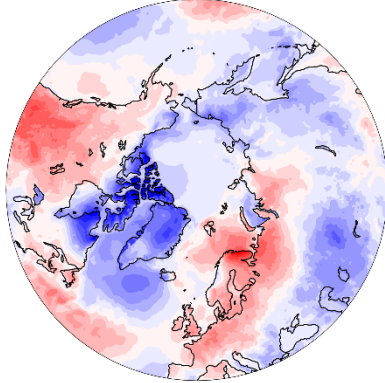
(a) T_{2m} : NAO positive minus negative



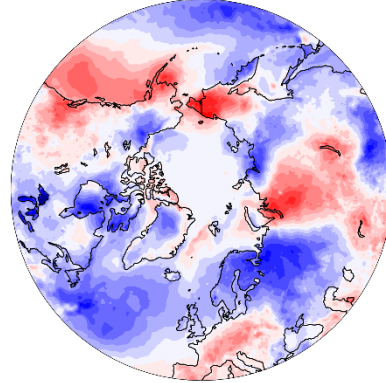
(b) T_{2m} : PDO positive minus negative



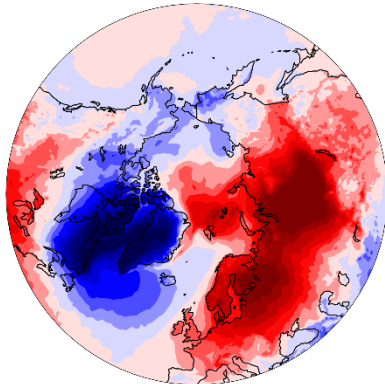
(c) T_{2m} JJA: NAO positive minus negative



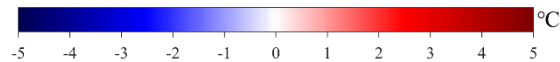
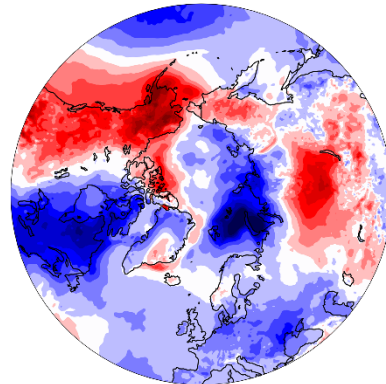
(d) T_{2m} JJA: PDO positive minus negative



(e) T_{2m} DJF: NAO positive minus negative



(f) T_{2m} DJF: PDO positive minus negative

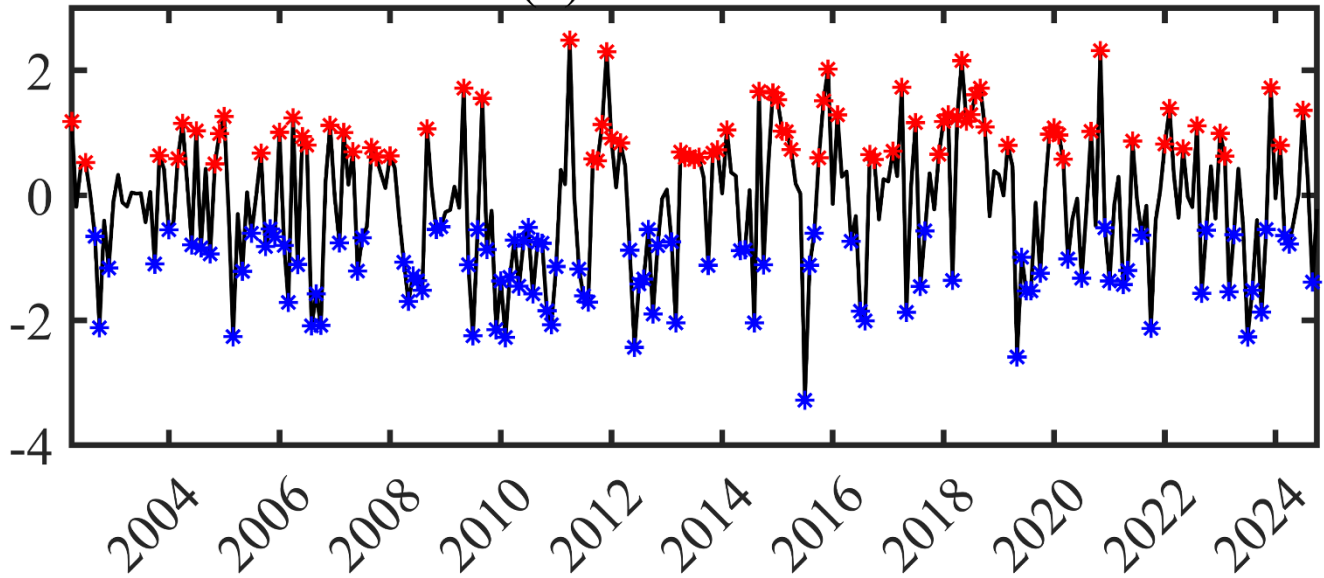


150

Figure S26: Near-surface air-temperature anomalies related to unsummed NAO and PDO indices. ERA5 2 m air-temperature anomalies over the Arctic for 2002–2024. Panels show differences between positive and negative NAO phases for all seasons (a), boreal summer (c) and boreal winter (e), and between positive and negative PDO phases for all seasons (b), boreal summer (d) and boreal winter (f). Positive and negative phases are defined as months when the normalized NAO or PDO index is greater than +0.5 or less than -0.5 (Fig. S27), respectively. Anomalies are calculated relative to the 1971–1999 monthly climatology.

155

(a) NAO index



(b) PDO index

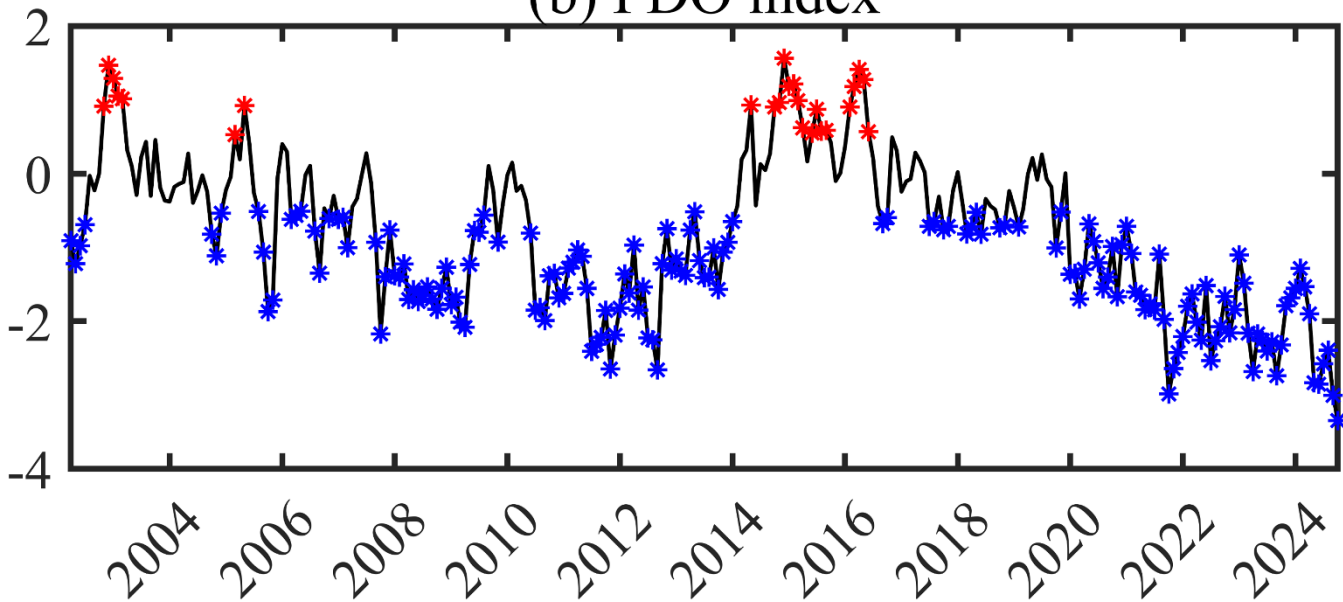


Figure S27: Raw climate indices showing positive and negative phases. Normalized monthly NAO and PDO indices over 2002–2024. Positive phases, shown in red, and negative phases, shown in blue, are defined as months when the normalized index is greater than +0.5 or less than -0.5, respectively. The NAO is shown in the upper panel and the PDO in the lower panel.

Table S1. GRACE hydrological correction estimates for RGI regions derived from GLDAS v2.1, PCR-GLOBWB 2, and CLM5.0

RGI regions	Hydrology model [Gt yr ⁻¹]			Model spread [Gt yr ⁻¹]	Hydrology uncertainty [Gt yr ⁻¹]
	GLDAS v2.1(Rodell et al., 2004)	PCR-GLOBWB 2(Sutanudjaja et al., 2018)	CLM 5.0(Lawrence et al., 2019)+GLDAS v2.1		
Alaska (ALA)	0.1 ± 3	1.8 ± 3	0.3 ± 1	1.7	± 3.4
Arctic Canada North (ACN)	0.2 ± 0	0.5 ± 0	0.5 ± 1	0.3	± 0.3
Arctic Canada South (ACS)	-0.9 ± 0	0.9 ± 1	0.2 ± 1	1.8	± 1.8
Iceland (ICE)	0.3 ± 0	0.2 ± 0	0.0 ± 0	0.3	± 0.3
Svalbard (SVA)	0.3 ± 0	0.9 ± 0	0.0 ± 0	0.6	± 0.6
Scandinavia (SCA)	0.0 ± 1	0.0 ± 2	-0.1 ± 1	0.1	± 1.0
Russian Arctic (RA)	0.2 ± 0	1.2 ± 0	0.0 ± 1	1.0	± 1.0
Arctic total	-0.1 ± 3	5.5 ± 4	0.9 ± 2	5.6	± 6.4
Western Canada US	-4.9 ± 4	1.1 ± 4	0.6 ± 7	6.0	± 7.2
North Asia	0.1 ± 0	0.3 ± 0	1.6 ± 4	1.5	± 1.5
Central Europe	0.0 ± 0	-0.3 ± 0	0.3 ± 1	0.3	± 0.3
Caucasus Middle East	-1.9 ± 0	-0.7 ± 0	-1.0 ± 1	1.2	± 1.2
High Mountain Asia	-1.9 ± 3	7.0 ± 2	6.5 ± 3	8.9	± 9.4
Low Latitudes	-0.1 ± 1	-2.6 ± 1	-0.6 ± 2	2.5	± 2.7
Southern Andes	-2.0 ± 1	-9.5 ± 1	-1.8 ± 2	7.5	± 7.6
New Zealand	-0.6 ± 0	-1.3 ± 0	-0.2 ± 1	0.7	± 0.7
Global total	-11.1 ± 6	-0.5 ± 6	6.3 ± 9	17.4	± 18.4

Notes: GLDAS v2.1 was used as the primary hydrological correction. Model spread is defined as the maximum absolute difference between the GLDAS-based correction trend and the alternative correction trends derived from PCR-GLOBWB 2 and CLM5.0. Hydrology uncertainty is computed as the quadrature sum of the GLDAS correction uncertainty and the model spread. The PCR-GLOBWB 2 estimates are taken from ref.([Wouters et al., 2019](#)). The CLM5.0 + GLDAS v2.1 values represent the mean of the CLM5.0- and GLDAS v2.1-based estimates following ref.([Ciraci et al., 2020](#)). Uncertainties are reported as 95% confidence intervals.

170 **Table S2. Autocorrelation significance of correlations between ICA-derived glacier modes and cumulative and non-cumulative climate indices**

Pair	Period	Pearson r	Effective DOF	Monte Carlo p
IC1-NAO $_{\Sigma}$	Full	-0.84	1.38	0.004
	Pre-gap	-0.91	1.00	0.001
	Post-gap	0.33	5.08	0.321
IC1-NAO (non-cumulative)	Full	-0.03	145.46	0.721
	Pre-gap	-0.05	100.63	0.639
	Post-gap	0.11	44.12	0.462
IC2-PDO $_{\Sigma}$	Full	0.85	6.48	<0.001
	Pre-gap	0.80	4.34	0.001
	Post-gap	0.90	1.00	0.001
IC2-PDO (non-cumulative)	Full	0.19	21.34	0.339
	Pre-gap	0.06	16.65	0.789
	Post-gap	0.74	6.34	0.002

Notes: Pearson r is the lag-zero correlation coefficient. Effective DOF is the autocorrelation-adjusted effective degrees of freedom, estimated from the lag-1 autocorrelation of the paired series. Monte Carlo p is the empirical significance level from surrogate Monte Carlo tests using independent AR(1) realizations. NAO $_{\Sigma}$ and PDO $_{\Sigma}$ denote the cumulative NAO and PDO indices; non-cumulative denotes the corresponding raw monthly indices. The pre-gap period corresponds to months 1–184 (2002.04–2017.07) and the post-gap period to months 195–271 (2018.06–2024.10). Values smaller than 0.001 are shown as <0.001.

175

Table S3. Fisher-z tests for differences between pre-gap and post-gap correlations of ICA-derived glacier modes with cumulative and non-cumulative climate indices

Comparison	Fisher-z statistic	Two-side <i>P</i>
IC1–NAO _Σ , pre-gap vs post-gap	-13.60	<0.001
IC2–PDO _Σ , pre-gap vs post-gap	-2.73	0.006
IC1–NAO, pre-gap vs post-gap	-1.10	0.269
IC1–PDO, pre-gap vs post-gap	-6.45	<0.001

180 Notes: Fisher-z tests were used to evaluate whether the pre-gap and post-gap correlation coefficients differ significantly for each ICA mode–climate index pair. NAO_Σ and PDO_Σ denote the cumulative NAO and PDO indices, whereas NAO and PDO denote the corresponding raw monthly indices. The pre-gap period corresponds to months 1–184 (2002.04–2017.07) and the post-gap period to months 195–271 (2018.06–2024.10) of the GRACE/GRACE-FO record. Reported *P* values are two-sided; values smaller than 0.001 are shown as <0.001.

185 **Table S4. Hector-derived noise characteristics and trend uncertainties for regional Arctic GIC mass anomalies (Eq. 1)**

RGI regions	Trend_white (Gt yr ⁻¹)	Trend_corr (Gt yr ⁻¹)	Scale Factor	Spectral index κ
Alaska (ALA)	-68.1 ± 1.4	-69.1 ± 20.4	14.6	-1.70
Arctic Canada North (ACN)	-37.5 ± 0.8	-34.5 ± 10.6	13.2	-1.69
Arctic Canada South (ACS)	-25.9 ± 0.5	-23.6 ± 5.6	11.2	-1.68
Iceland (ICE)	-6.9 ± 0.2	-7.1 ± 1.6	8.0	-1.12
Svalbard (SVA)	-18.7 ± 0.8	-20.4 ± 6.2	7.8	-1.50
Scandinavia (SCA)	0.7 ± 0.1	0.7 ± 0.6	6.0	-0.82
Russian Arctic (RA)	-15.5 ± 0.5	-16.0 ± 5.2	10.4	-1.70

Notes: Trend_white denotes the linear mass-change rate estimated under a pure white-noise assumption, whereas Trend_corr is the corresponding trend when time-correlated (power-law + white) noise is accounted for. Scale factor is the multiplicative factor by which the formal white-noise uncertainty must be inflated to obtain the corrected trend uncertainty. Spectral index κ is the spectral slope of the power-law noise, where more negative κ indicates stronger low-frequency correlation. All reported trend uncertainties correspond to the 95% confidence interval.

190 **Table S5. Trend uncertainties for regional Arctic GIC mass anomalies from the climate-index regression including NAO_{Σ} and PDO_{Σ} (Eq. 7)**

RGI regions	Trend_white (Gt yr ⁻¹)	Trend_corr (Gt yr ⁻¹)	Scale Factor
Alaska (ALA)	-87.8 ± 3.5	-92.3 ± 15.5	4.4
Arctic Canada North (ACN)	-26.9 ± 1.9	-27.7 ± 8.0	4.2
Arctic Canada South (ACS)	-23.4 ± 1.4	-23.0 ± 5.8	4.1
Iceland (ICE)	-6.1 ± 0.7	-5.9 ± 1.4	2.0
Svalbard (SVA)	-17.1 ± 1.4	-17.4 ± 6.3	4.5
Scandinavia (SCA)	0.5 ± 0.6	0.4 ± 0.9	1.5
Russian Arctic (RA)	-14.0 ± 1.2	-14.0 ± 2.1	1.8

Notes: Trends were estimated using the climate-index regression in Equation (7), in which the linear trend terms, NAO_{Σ} and PDO_{Σ} were solved simultaneously. Trend_white denotes the residual linear trend and its uncertainty estimated under a pure white-noise assumption. Trend_corr denotes the corresponding trend and uncertainty estimated from the full regression covariance under an AR(1) residual-noise model. The scale factor is the multiplicative factor by which the formal white-noise uncertainty is inflated to obtain the AR(1)-corrected trend uncertainty. All reported trend uncertainties correspond to the 95% confidence interval.

195

Table S6. GRACE/GRACE-FO glacier mass budgets and uncertainty contributions for RGI regions

RGI regions	Mass balance Gt yr ⁻¹	correlated-noise regression uncertainty Gt yr ⁻¹	GIA uncertainty Gt yr ⁻¹	Hydrology correction Gt yr ⁻¹	Noise error Gt yr ⁻¹	Leakage error Gt yr ⁻¹	Processing-center spread Gt yr ⁻¹
Alaska (ALA)	-69.1 ± 20.9	-69.0 ± 20.4	± 0.0	0.1 ± 3.5	± 0.3	± 2.8	± 1.0
Arctic Canada North (ACN)	-34.5 ± 15.7	-34.3 ± 10.6	± 5.0	0.2 ± 0.3	± 0.1	± 9.4	± 4.7
Arctic Canada South (ACS)	-23.6 ± 15.4	-24.5 ± 5.6	± 2.0	-0.9 ± 1.8	± 0.1	±14.1	± 0.3
Iceland (ICE)	-7.1 ± 2.2	-6.8 ± 1.6	± 1.0	0.3 ± 0.3	± 0.1	± 0.6	± 0.9
Svalbard (SVA)	-20.4 ± 7.9	-20.1 ± 6.2	± 1.0	0.3 ± 0.6	± 0.2	± 2.2	± 4.2
Scandinavia (SCA)	0.7 ± 4.2	0.7 ± 0.6	± 4.0	0.0 ± 1.0	± 0.1	± 0.4	± 0.6
Russian Arctic (RA)	-16.0 ± 7.2	-15.8 ± 5.2	± 3.0	0.2 ± 1.0	± 0.2	± 3.2	± 2.2
Arctic total	-169.7 ± 32.8	-169.8 ± 25.1	± 7.0	-0.1 ± 6.4	± 0.5	± 17.6	± 6.8
Western Canada US	-13.2 ± 20.8	-18.1 ± 18.4	± 5.0	-4.9 ± 7.2	± 0.1	± 1.5	± 3.9
North Asia	1.2 ± 4.4	1.3 ± 3.2	± 2.0	0.1 ± 1.5	± 0.2	± 1.2	± 1.2
Central Europe	-1.5 ± 1.4	-1.5 ± 1.2	± 0.0	0.0 ± 0.3	± 0.1	± 0.6	± 0.4
Caucasus Middle East	-5.0 ± 3.9	-6.9 ± 2.8	± 0.1	-1.9 ± 1.2	± 0.1	± 1.5	± 1.9
High Mountain Asia	-23.8 ± 16.8	-25.7 ± 10.6	± 5.0	-1.9 ± 9.4	± 0.2	± 4.1	± 6.3
Low Latitudes	1.0 ± 4.8	0.9 ± 2.2	± 2.0	-0.1 ± 2.7	± 0.1	± 1.1	± 2.4
Southern Andes	-20.6 ± 11.0	-22.6 ± 4.4	± 4.0	-2.0 ± 7.6	± 0.2	± 3.9	± 3.7
New Zealand	0.1 ± 1.7	-0.5 ± 0.8	± 1.0	-0.6 ± 0.7	± 0.1	± 0.5	± 0.8
Global total	-231.8 ± 45.5	-242.9 ± 33.5	± 11.4	-11.1 ± 18.4	± 0.8	± 18.7	± 11.3

Notes: Mass balance is the final GRACE/GRACE-FO glacier mass-change rate after applying the primary GLDAS v2.1 hydrological correction.

200 The correlated-noise regression uncertainty accounts for temporal correlation in the GRACE/GRACE-FO time series. GIA uncertainty is included as a literature-based model uncertainty only, because all mascon products already include GIA corrections. Hydrological-correction uncertainty is estimated from the sensitivity of regional corrections to GLDAS v2.1, PCR-GLOBWB 2 and CLM5.0-based estimates. Noise and leakage errors are propagated from the GSFC mascon uncertainty fields, with leakage including both stochastic leakage and deterministic leakage-trend

components. Processing-center spread is defined from the spread of regional trends estimated independently from the CSR, JPL and GSFC
205 mascon products. Total mass-balance uncertainty is computed as the quadrature sum of all listed uncertainty contributions. All uncertainties are
reported as 95% confidence intervals.

Table S7 Sensitivity of the time-differenced regression to smoothing-window choice across Arctic glacier regions

RGI regions	Selected window (months)	AbsDiff_pct (%)	RMSE (Gt)	Corr
Alaska (ALA)	25	3	33	0.97
Arctic Canada North (ACN)	25	2	6	0.99
Arctic Canada South (ACS)	43	2	7	0.95
Iceland (ICE)	13	4	9	0.44
Svalbard (SVA)	25	1	13	0.96
Scandinavia (SCA)	13	142	3	0.98
Russian Arctic (RA)	31	33	8	0.94

Note: For each region, the preferred running-mean window was selected from 13, 25, 31, 37, 43 and 55 months as that minimizing the absolute difference in cumulative climate-related mass change relative to the corresponding undifferenced regression solution. AbsDiff_pct denotes the absolute percentage difference in cumulative climate-related mass change between the differenced and undifferenced solutions over their common analysis period. RMSE and Corr denote the root mean square difference and Pearson correlation, respectively, between the reconstructed climate-related component from the differenced regression and that estimated from the undifferenced regression.

215 SI References

- Ciraci, E., Velicogna, I., and Swenson, S.: Continuity of the Mass Loss of the World's Glaciers and Ice Caps From the GRACE and GRACE Follow-On Missions, *Geophysical Research Letters*, 47, e2019GL086926, <https://doi.org/10.1029/2019gl086926>, 2020.
- Lawrence, D. M., Fisher, R. A., Koven, C. D., Oleson, K. W., Swenson, S. C., Bonan, G., Collier, N., Ghimire, B., van Kampenhout, L., Kennedy, D., Kluzek, E., Lawrence, P. J., Li, F., Li, H., Lombardozzi, D., Riley, W. J., Sacks, W. J., Shi, M., Vertenstein, M., Wieder, W. R., Xu, C., Ali, A. A., Badger, A. M., Bisht, G., van den Broeke, M., Brunke, M. A., Burns, S. P., Buzan, J., Clark, M., Craig, A., Dahlin, K., Drewniak, B., Fisher, J. B., Flanner, M., Fox, A. M., Gentine, P., Hoffman, F., Keppel-Aleks, G., Knox, R., Kumar, S., Lenaerts, J., Leung, L. R., Lipscomb, W. H., Lu, Y., Pandey, A., Pelletier, J. D., Perket, J., Randerson, J. T., Ricciuto, D. M., Sanderson, B. M., Slater, A., Subin, Z. M., Tang, J., Thomas, R. Q., Val Martin, M., and Zeng, X.: The Community Land Model Version 5: Description of New Features, Benchmarking, and Impact of Forcing Uncertainty, *Journal of Advances in Modeling Earth Systems*, 11, 4245-4287, <https://doi.org/10.1029/2018MS001583>, 2019.
- 220 Rodell, M., Houser, P. R., Jambor, U., Gottschalck, J., Mitchell, K., Meng, C. J., Arsenault, K., Cosgrove, B., Radakovich, J., Bosilovich, M., Entin, J. K., Walker, J. P., Lohmann, D., and Toll, D.: The global land data assimilation system, *Bulletin of the American Meteorological Society*, 85, 381–394, <https://doi.org/10.1175/bams-85-3-381>, 2004.
- 225 Sutanudjaja, E. H., van Beek, R., Wanders, N., Wada, Y., Bosmans, J. H. C., Drost, N., van der Ent, R. J., de Graaf, I. E. M., Hoch, J. M., de Jong, K., Karssenber, D., López López, P., Peßenteiner, S., Schmitz, O., Straatsma, M. W., Vannamettee, E., Wisser, D., and Bierkens, M. F. P.: PCR-GLOBWB 2: a 5 arcmin global hydrological and water resources model, *Geosci. Model Dev.*, 11, 2429-2453, <https://doi.org/10.5194/gmd-11-2429-2018>, 2018.
- 230 Wouters, B., Gardner, A. S., and Moholdt, G.: Global Glacier Mass Loss During the GRACE Satellite Mission (2002-2016), *Frontiers in Earth Science*, 7, 96, <https://doi.org/10.3389/feart.2019.00096>, 2019.